Working models for spatial distribution and level of Mars' seismicity

M. Knapmeyer,[1] J. Oberst,[1] E. Hauber,[1] M. Wählisch,[1] C. Deuchler,[1] and R. Wagner[1]

Received 3 March 2006; revised 14 June 2006; accepted 30 June 2006; published 18 November 2006.

[1] We present synthetic catalogs of Mars quakes, intended to be used for performance assessments of future seismic networks on the planet. We have compiled a new inventory of compressional and extensional tectonic faults for the planet Mars, comprising 8500 faults with a total length of 680,000 km. The faults were mapped on the basis of Mars Orbiting Laser Altimeter (MOLA) shaded relief. Hence we expect to have assembled a homogeneous data set, not biased by illumination and viewing conditions of image data. Updated models of Martian crater statistics and geological maps were used to assign new maximum ages to all faults. On the basis of the fault catalog, spatial distributions of seismicity were simulated, using assumptions on the available annual seismic moment budget, the moment-frequency relationship, and a relation between rupture length and released moment. We have constructed five different models of Martian seismicity, predicting an annual moment release between 3.42×10^{16} Nm and 4.78×10^{18} Nm and up to 572 events with magnitudes greater than 4 per year as upper limit end-member case. Most events are expected on the Tharsis shield, but minor seismic centers are expected south of Hellas and north of Utopia Planitia.

Citation: Knapmeyer, M., J. Oberst, E. Hauber, M. Wählisch, C. Deuchler, and R. Wagner (2006), Working models for spatial distribution and level of Mars' seismicity, *J. Geophys. Res.*, *111*, E11006, doi:10.1029/2006JE002708.

1. Introduction

[2] Seismological observations on future missions to Mars are a crucial step to further our understanding of planetary dynamics [e.g., *Stevenson*, 2001; *Lognonné*, 2005]. Determination of the planet's core size [e.g., *Sohl and Spohn*, 1997], detection of mineralogical phase transitions [e.g., *Mocquet et al.*, 1996] and local measurements of crustal thickness as an anchor for gravity based models, as suggested, e.g., by *Zuber et al.* [2000] and *Zuber* [2001], are among the foremost goals. However, to optimize the science performance of a seismic experiment, the stations must be placed at carefully selected positions.

[3] While the distribution of quakes is unknown, it is desirable to have at least a physically meaningful working model for the spatial distribution and level of global seismicity as a basis for the planning of future seismic experiments. Clues on the distribution of today's seismicity may be obtained from the abundance of the many tectonic faults visible on the surface, believed to be expressions of internal forces and stress fields [e.g., *Carr*, 1974; *Wise et al.*, 1979; *Carr*, 1981; *Banerdt et al.*, 1992]. Many mapping campaigns have been made; however, unbiased global inventories (which depend critically on the quality and resolution of the available image data, as well as on viewing and illumination conditions) are difficult to obtain for a planet as large as Mars. Most mapping efforts concentrated on features of local extent [*Tanaka and Davis*, 1988; *Tanaka*, 1990; *Dohm and Tanaka*, 1999; *Hauber and Kronberg*, 2001, 2005; *Anderson et al.*, 2004] and prominent regional fault systems like those on the Tharsis bulge [e.g., *Plescia and Saunders*, 1982; *Tanaka et al.*, 1991; *Banerdt et al.*, 1992]. *Anderson et al.* [2001] undertook a comprehensive study of faults on the western hemisphere of Mars using Viking Orbiter imagery, including almost 24,500 individual faults. A follow-up mapping effort covering the eastern hemisphere is currently under way [*Pounders et al.*, 2002].

[4] Another important constraint for mission design is the number and size of the quakes that can be expected. The only planetary bodies for which we have quantitative results for the level of seismicity are the Earth and the Moon, which show very different seismic activity. The average seismic moment release of the Earth in the years 1984–2003 was $\approx 4 \times 10^{21}$ Nm per year, according to the Harvard Centroid Moment Tensor catalog (available at http://www.seismology.harvard.edu/projects/CMT/) [*Dziewonski and Woodhouse*, 1983; *Dziewonski et al.*, 1983] (also see annual updates of the CMT). The annual moment release of the Moon as determined from the shallow moonquakes is between 10^{14} Nm and 10^{15} Nm only [*Oberst*, 1987].

[5] The beginning of the seismicity modeling of Mars dates back to *Anderson et al.* [1972] who suggest that the level of seismicity of Mars is between that of the Moon and Earth. From the results of the Viking seismic experiment, *Anderson et al.* [1977] conclude that the nondetection of quakes does indeed show that the Martian seismicity per unit area is smaller than that of Earth with 95% probability.

[6] In a study for the assessment phase of the Mesur/MarsNet project, *Phillips* [1991] suggests that global differential cooling of the lithosphere may produce an annual moment release of about 4.8×10^{18} Nm. This theoretical

[1]German Aerospace Center, Institute of Planetary Research, Berlin, Germany.

0148-0227/06/2006JE002708

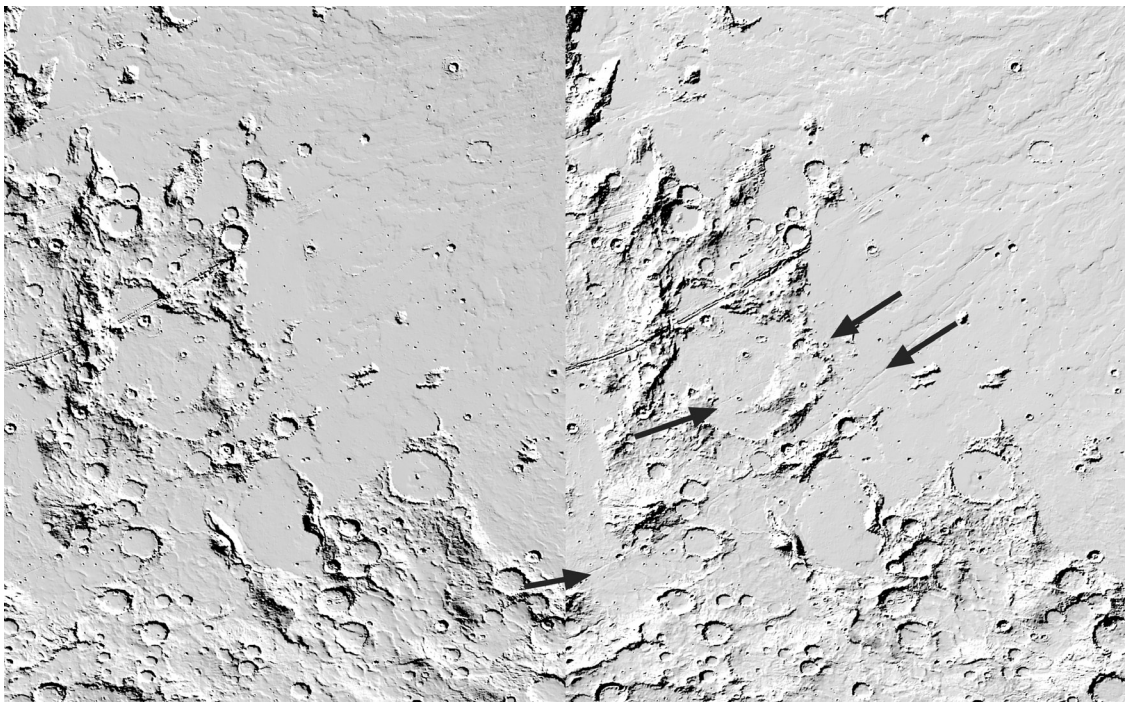

Figure 1. MOLA-based shaded relief images, artificially illuminated from (left) NE and (right) NW. Faults stretching from NE to SW can only be seen if illuminated from NW (see arrows).

estimate is complemented by *Golombek et al.* [1992] and *Golombek* [2002], who estimate the moment release from the total slip on faults visible on the surface. Considering all uncertainties, *Golombek et al.* [1992] give a lower estimate of about 10^{18} Nm, whereas *Golombek* [2002] brackets the annual budget between 10^{17} Nm and 10^{19} Nm.

[7] Results from the recent Mars missions as well as recent developments in Earthquake statistics in general now allow to derive new estimates for the annual budget, the size-frequency distributon and the expected spatial distribution of quakes on Mars.

[8] For the purpose of seismic modeling, we compiled a new global catalogue of tectonic fault systems. Our main goal was to obtain a homogeneous data set as far as possible, which is why we used MOLA (Mars Orbiting Laser Altimeter) shaded relief maps instead of images to identify the faults, thereby avoiding bias by source data quality, viewing and illumination conditions. To obtain reliable maximum ages for each fault, we updated the age assignments for geologic units of the planet. We then developed algorithms that allow us to tie fault distributions to current seismicity, following the global lithospheric cooling approach of *Phillips* [1991]. On the basis of the tectonic fault catalog, we derived synthetic catalogs of Mars quakes, which may be used for performance studies of future seismic networks.

2. Methods

2.1. Mapping Procedure

[9] The Mars Orbiting Laser Altimeter (MOLA) which operated on board the Mars Global Surveyor from 1997 to 2001 has mapped the planet with high precision and consistency [*Smith et al.*, 2001, 2003]. Global topographic MOLA maps (interpolated from the individual altimeter tracks) available in 4 separate sheets in simple cylindrical projections at 64 pixels/deg (0.926 km/pixel) were downloaded from http://pds-geosciences.wustl.edu/missions/mgs/megdr.html. The four sheets were mosaicked, resampled to 1 km/pixel, shaded, and converted to Mercator and stereographic (for areas beyond ±60° of latitude) projections for the measurements.

[10] The identification and positional measurements of tectonic faults were carried out interactively on the computer screen. Specifically, the topographic maps were artificially illuminated from two viewing directions 90° apart (at azimuths 45° and 315°), to avoid that faults of specific orientations would be overrepresented or missed in our catalog (Figure 1). Hence, contrary to mapping on the basis of images, where the light conditions have to be taken as is, we were able to carry out the mapping under ''controlled conditions'' and thus could avoid any sampling bias. We mapped faults down to a minimum length of 4 km, corresponding to 4 pixels. This is at the resolution limit of the data, but since the number of faults that short is very limited, we do not expect that possible misinterpretations produce any significant bias in our results. Each surface fault was stored in a set of equally spaced (250 m) sections on the MOLA reference sphere. The fault coordinates were converted back to the original simple cylindrical projection for visualization.

[11] Only thrust faults and normal faults were mapped. Previous studies found that the overwhelming majority of faults on Mars are either normal faults due to tension or thrust faults due to compression. Only few strike-slip faults were unambiguously identified [*Schultz*, 1989; *Anguita et al.*, 2001; *Tanaka et al.*, 2003; *Okubo and Schultz*, 2004; *Artita*

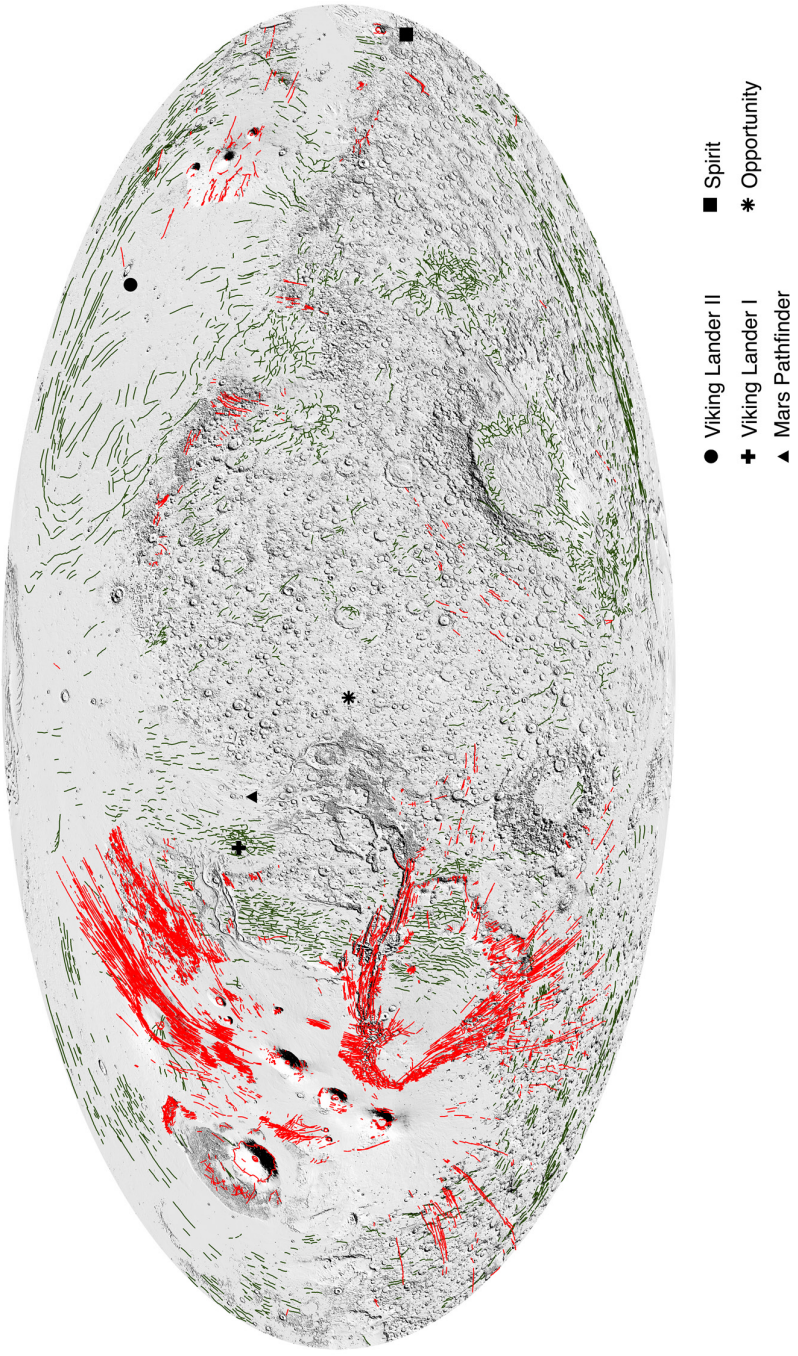

Figure 2. Global distribution of extensional (red) and compressional (green) faults on Mars.

and Schultz, 2005]. Since strike-slip faults on Earth are a typical product of plate tectonics, the almost complete lack of this fault type is not surprising for Mars, which is considered to be a one-plate planet. Though areas on Mars have large contiguous systems of faults, we do not store information on ''fault linkage'' [e.g., *Mansfield and Cartwright*, 2001; *Peacock*, 2002]; every fault is treated as individual.

[12] Normal faults in extensional settings are widespread on Mars and often grouped in fault sets with a particular trend pattern, e.g., radiating outward from a tectonic center. [*Anderson et al.*, 2001]. Where the normal faults occur in pairs and constitute a tectonic graben, their identification is particularly straightforward. Typical examples of this kind are very long and narrow grabens, which often occur in sets and radiate from specific centers in Tharsis. In the more complex Martian extensional structures, asymmetric grabens or half grabens are common [e.g., *Hauber and Kronberg*, 2001, 2005]. Therefore the identification of a linear topographic scarp as a normal fault associated with a half graben is straightforward if it is associated with such a complex extensional structure, but more ambiguous if it occurs as an isolated feature.

[13] We mapped two types of landforms related to crustal shortening on Mars: wrinkle ridges and lobate scarps (see *Mueller and Golombek* [2004] for a recent review on Martian contractional surface features). Wrinkle ridges consist of two morphological elements, a broad arch of low relief and a superposed, narrow, crenulated ridge (''wrinkle'') [e.g., *Strom*, 1972a, 1972b; *Bryan*, 1973; *Maxwell et al.*, 1975]. They are thought to be the surface expression of blind thrusts at depth and folding of near-surface layered material [e.g., *Schultz*, 2000a, and references therein]. Wrinkle ridges are common on all terrestrial planets, and have been found in many locations on Mars [*Chicarro et al.*, 1985]. A concentric set of wrinkle ridges around the Tharsis region dominates the pattern of contractional features in the western hemisphere of Mars (Figure 2). Other prominent populations of wrinkle ridges exist in Hesperia Planum and on the floors of large impact basins like Isidis [*Chicarro et al.*, 1985; *Mueller and Golombek*, 2004]. Since wrinkle ridges are quite large, with lengths of tens to hundreds of kilometers, widths of up to several tens of kilometers, and heights of tens to hundreds of meters and therefore well above the uncertainty of MOLA measurements, they can easily be detected in MOLA data [*Golombek et al.*, 2001].

[14] Lobate scarps with length of tens to hundreds of kilometers and scarp heights of up to several hundreds of meters are interpreted as thrust faults which rupture the surface [e.g., *Watters*, 1993]. They are also large enough to be detected in MOLA data. They occur mainly in the highlands, e.g., in Terra Cimmeria and Arabia Terra [*Watters*, 2003], and are often oriented roughly parallel to the Martian dichotomy boundary [*Watters and Robinson*, 1999].

[15] All mapping data were derived and conveniently stored in the Geographic Information System (GIS) GRASS (Geographic Resources Analysis Support System), which has become a popular tool in planetary science [*Frigeri et al.* 2002; *Deuchler et al.*, 2004] as it makes various analyses across different data sets straightforward.

2.2. Geologic Map and Age Assignments

2.2.1. Impact Cratering Chronology of Mars

[16] Crater frequency measurements make use of the simple principle that the number of craters in a given area is directly linked to its exposition time toward the projectile flux: the more craters, the higher the age.

[17] In a first stage, measurements of crater frequencies provide relative ages which are given as cumulative frequencies equal to, or larger than, a reference diameter; commonly used are diameters of 1 km and 10 km. In order to derive the relative age of a given geologic unit, the crater production function polynomial derived by *Neukum et al.* [2001] and *Ivanov* [2001] is fitted to the measured crater size-frequency distribution by using the method of least squares, to compute the cumulative frequency at the reference diameter(s). This frequency represents the relative crater retention age of a geologic unit. The uncertainties introduced by this method is on the order of 20–30%, dependent of the number of craters and of the size of the measurement area.

[18] The second step uses an impact chronology model to derive absolute ages. For the Earth's moon, a chronology model could be established by calibrating radiometric ages of lunar rock. Since no rock materials of known origin locations are available until now from the surface of Mars, the cratering rate can only be estimated by interplanet comparisons of the relative projectile flux. The current impact cratering chronology model for Mars which emerged from earlier versions [*Hartmann et al.*, 1981; *Neukum and Wise*, 1976; *Neukum and Hiller*, 1981] is based on Mars/Moon cratering rate ratios calculated from the observed flux of planet-crossing asteroids and their size distribution [*Ivanov*, 2001; *Hartmann and Neukum*, 2001]. The resulting cumulative frequency for a reference diameter of 1 km versus time will be shown in section 3.1, where the variation of fault production with time is discussed.

2.2.2. Dating of Faults

[19] Constraints on the time of formation of a fault may come from the age of the geologic unit on which the fault is located, because the fault must be younger than the ruptured rock. However, as the fault can have formed any time after the emplacement of the geologic unit, these ages represent only maximum ages.

[20] An attempt was made to assign each fault sections to a specific geological unit and a respective maximum time of formation. The geologic units for each fault were identified using the global 1:15,000,000 scale geologic map of Mars [*Scott et al.*, 1986, 1987a, 1987b], available in digital form in a resolution of 32 pixel/deg. The map shows 93 distinct geological units in the established Martian stratigraphic system [*Tanaka*, 1986; *Tanaka et al.*, 1992]. The map had been compiled on the MDIM 1.0 base map [*Kirk et al.*, 2000], which is considered outdated today. Hence, to remove the main geometric offsets with respect to the MOLA shaded relief, the map was shifted in longitude to conform with the currently adopted prime meridian, and reprojected onto a reference sphere with radius of 3396 km.

[21] To express age relationships, the cumulative frequencies of craters equal to, or larger than, 10 km in diameter are conveniently given in this map for each geologic unit. Coincidentally, the very early impact cratering chronology model for Mars [*Hartmann et al.*, 1981; *Neukum and Wise*,

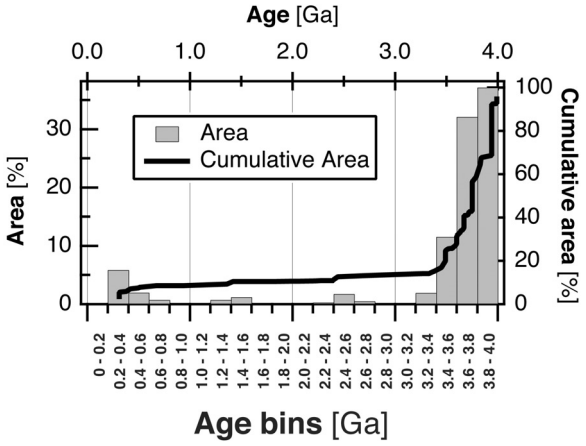

Figure 3. Fraction of the Mars surface within given age limits. Seventy-five percent of the surface are older than 3.5 Ga.

1976; *Neukum and Hiller*, 1981] was updated recently. Specifically, new polynomial coefficients for the Martian crater production function and new Mars/Moon cratering rate ratios over time were calculated from the currently observed flux of planet-crossing asteroids [*Ivanov*, 2001; *Hartmann and Neukum*, 2001]. Hence we extracted the frequency of 1 km craters from this updated polynomial model, and were able to assign new ages to the geologic provinces in the geologic map. Thus an age of 3.99 Ga was assigned to the oldest units on Mars (Figure 3).

2.3. Seismicity Model

[22] Our seismicity model consists of three parts: (1) an estimation of the annual seismic moment budget, (2) the subdivision of this budget into individual quakes that follow a certain moment-frequency-distribution, and (3) the assignment of these individual quakes to faults from our fault catalogue, according to a relation between rupture length and released seismic moment which we derive on the basis of the constant stress drop hypothesis. A threshold surface age is used as simple proxy to distinguish between seismically active and inactive faults, using the fault ages as modeled above.

2.3.1. Basic Assumptions

[23] The basic assumption of our seismicity simulation is that global contraction of Mars due to cooling of the lithosphere is the main source of tectonic (''thermoelastic'') stress today [*Phillips*, 1991]. Sudden stress releases, i.e., seismic events, are assumed to occur on the observed visible tectonic fault systems only: No new faults are produced. For simplicity, it is assumed that all quakes occur at the surface (most deep quakes on Earth occur in subducted slabs, which do not exist on the one-plate planet Mars). We permit that quakes occur repeatedly on the same faults, an observation which is not uncommon on Earth and is explained by the stick-slip behavior of the spring-slider model [e.g., *Scholz*, 2003]. The probability of occurrence of a quake is assumed to be equal on all faults.

[24] Owing to our lack of deeper knowledge on the dynamics of the Martian crust, we do not model higher-order effects, as aftershock sequences or ''seismic gaps'' (where large quakes ''deactivate'' a part of the fault for some time, whereas stress on neighboring faults increases [e.g., *Westerhaus et al.*, 2002]). We also do not model origin times or sequencing of the quakes, only epicentral coordinates and seismic moments.

2.3.2. Annual Seismic Moment Budget

[25] The ''size'' of an earthquake is best described by the seismic moment M_0, which is defined as

$$M_0 = \int_A \mu S dA \tag{1}$$

[e.g., *Stacey*, 1992] where μ is the shear modulus (rigidity) of the ruptured rock, A is the rupture area and S is the slip on the rupture area. In real media, both shear modulus and slip can be functions of spatial coordinates. However, for the determination of the scalar moment it is sufficient to replace the slip function S by a spatially constant average slip $\overline{S}$, and to assume a homogeneous medium with constant shear modulus. Equation (1) then reduces to

$$M_0 = \mu \overline{S} A \tag{2}$$

Since most people are used to judge earthquakes by their magnitude, we introduce the moment magnitude

$$M_W = \frac{2}{3}(\log_{10} M_0 - 9.1) \tag{3}$$

[e.g., *Bormann et al.*, 2002], where M_0 is to be given in Newton meters (this magnitude definition is based on empirical relations found on Earth, but we suggest to keep it on Mars in order to avoid confusion by large differences in magnitude numbers for the same moment. However, the way magnitudes are computed from seismogram amplitudes needs to be adapted to the wave propagation characteristics of Mars.) The familiar terrestrial magnitude is used in tables and figures for the reader's convenience. All computations are based on the seismic moment.

[26] If M_0^i is the seismic moment of the ith quake, the cumulative moment of all quakes occurring in time range Δt is given by

$$M_{cum} = \sum_i M_0^i \tag{4}$$

This cumulative moment is connected to the strain rate $\dot{\varepsilon}$ by

$$M_{cum} = \eta \dot{\varepsilon} V \mu \Delta t \tag{5}$$

[*Phillips*, 1991; *Bratt et al.*, 1985], where V is the seismogenic volume and η, with $0 \leq \eta \leq 1$, is the seismic efficiency which describes how much of the strain is released in seismic events instead of aseismic deformation, such as folding or aseismic creep.

[27] The seismogenic volume is the volume of the seismogenic lithosphere and is assumed to be a spherical shell with its outer radius corresponding to the planetary radius R_P and a thickness H. The volume of such a shell is given by

$$V = \frac{4}{3}\pi\left[R_P^3 - (R_P - H)^3\right] \tag{6}$$

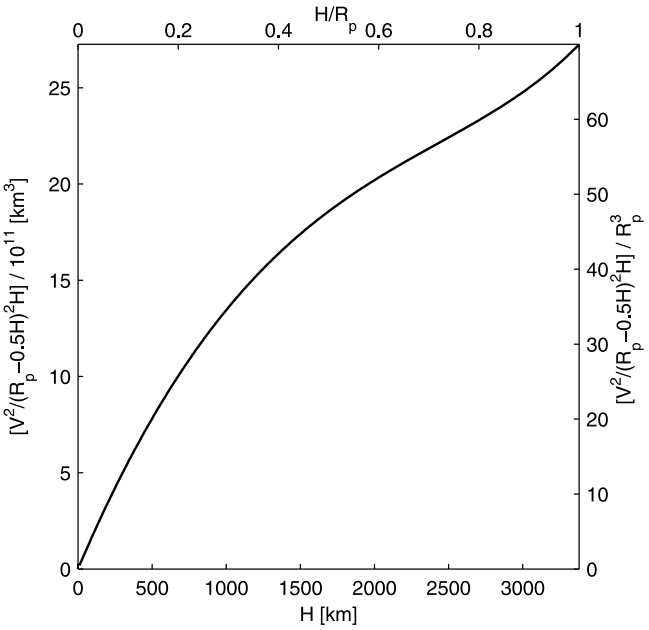

Figure 4. Dependency of M_{cum} on layer thickness H. Lower x axis and left y axis give absolute values. Top and right axes give dimensionless scales obtained by normalization with R_P and R_P^3, respectively.

The strain rate due to the thermal shrinking of the planet is given approximately by the shrinking of that shell. Following *Phillips* [1991], we therefore compute the strain rate as

$$\dot{\varepsilon} = \frac{1}{H\left(R_P - \frac{H}{2}\right)^2} \int_{R_P - H}^{R_P} \alpha \dot{T} r^2 dr \tag{7}$$

We assume that the thermal expansion coefficient α and the cooling rate $\overline{T}$ are constant throughout the entire seismic lithosphere. The integration can then be solved easily, and by inserting (6) we obtain

$$\dot{\varepsilon} = \frac{\alpha \dot{T} V}{4\pi H\left(R_P - \frac{H}{2}\right)^2} \tag{8}$$

Now (8) can be inserted into (5), and we get

$$M_{cum} = \eta \mu \alpha \dot{T} \Delta t \frac{V^2}{4\pi H\left(R_P - \frac{H}{2}\right)^2} \tag{9}$$

as the cumulative seismic moment per time interval Δt.

[28] For a small thickness H of the seismogenic lithosphere, the geometry term $V^2/4\,\pi\,H(R_P - H/2)^2$ is essentially a linear dependence on H as depicted in Figure 4, and the cumulative seismic moment is approximately proportional to H. However, we will use the linear approximation only as a rule of thumb and use the exact form (9) in all computations.

[29] Equation (9) is a lower limit for the cumulative moment due to thermal shrinking, since it considers only the contraction of the lithospheric shell. The total change of the planetary radius, however, is also influenced by the cooling of the entire mantle, a possibly freezing inner core and the solidification of partial melt. The importance of such effects for recent radius changes deserves a closer look in a future study.

2.3.3. Moment-Frequency Distribution

[30] The size-frequency-distribution of earthquakes is often [e.g., *Goins and Lazarewicz*, 1979; *Phillips*, 1991; *Stacey*, 1992; *Golombek et al.*, 1992; *Golombek*, 2002] described by the log linear Gutenberg-Richter distribution

$$\log_{10} N(M) = a - bM \tag{10}$$

where $N(M)$ is the number of quakes with magnitude equal to or larger than M; the numbers a and b are empirical parameters.

[31] This distribution can be correct only in a limited range of magnitudes. Toward small magnitudes, all quake catalogs are incomplete because of the limited sensitivity of seismometer networks. Any real catalog will therefore not follow the Gutenberg-Richter distribution for small magnitudes. For large magnitudes, the real frequency of large quakes must be significantly smaller than predicted by the Gutenberg-Richter distribution, since the finite size of planets and their finite energy budget do not allow for arbitrarily large quakes (conservation of momentum principle [e.g., *Kagan*, 2002b]).

[32] Additionally, the seismic moment should be used instead of magnitude, since the moment is the underlying physical quantity and does not suffer from the saturation effects known to exist in magnitude scales.

[33] *Kagan* [2002a] discusses several mathematical approaches for moment-frequency-distributions that are truncated on both left and right sides in different ways. From the current data, it cannot be judged which of these best reflects the physical process behind the observed distribution. We decided to use his "truncated Gutenberg-Richter distribution" (also named "truncated Pareto distribution") in which the probability density function $P(M)$, describing the probability of a quake of moment M, is truncated on both sides:

$$P(M) = \begin{cases} \dfrac{M_{\max}^{\beta} M_{\min}^{\beta}}{M_{\max}^{\beta} - M_{\min}^{\beta}} \beta M^{-1-\beta} & M_{\min} \le M \le M_{\max} \\ 0 & \text{otherwise} \end{cases} \tag{11}$$

In this equation, $M_{\min}$ is the smallest catalogued seismic moment and $M_{\max}$ is the largest possible seismic moment. Both $M_{\min}$ and $M_{\max}$ are hard boundaries, values outside the interval $[M_{\min}, M_{\max}]$ are not contained in the catalog. The slope parameter β is analogous to the b value in the original Gutenberg-Richter distribution. Since we use seismic moment instead of magnitude and because of equation (3), the relation between b and β is

$$\beta = \frac{2}{3} b \tag{12}$$

provided that the b value was determined from a distribution of moment magnitudes M_W. This relation must be accounted for when comparing different quake catalogs.

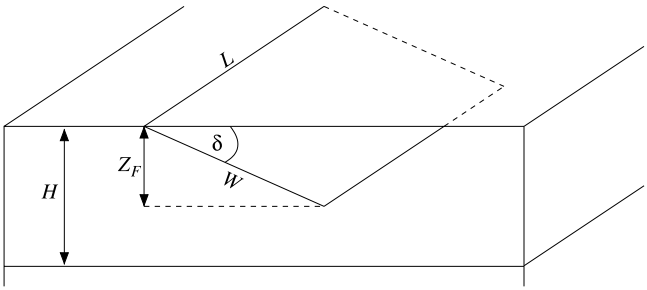

Figure 5. Fault geometry. H, seismogenic depth; Z_F, faulting depth; L, fault length on map; W, fault width; δ, fault dip angle. The same geometry applies to rupture areas.

[34] The fraction $N(M_0)$ of quakes with moment larger than M_0 for this distribution is given by

$$N(M_0) = \frac{\left(M_{\min}/M_0\right)^{\beta} - \left(M_{\min}/M_{\max}\right)^{\beta}}{1 - \left(M_{\min}/M_{\max}\right)^{\beta}} \quad \text{for } M_{\min} \le M_0 \le M_{\max} \tag{13}$$

[*Kagan*, 2002a].

[35] The lower boundary $M_{\min}$ is not a property of the seismotectonic regime but of the recording network. The cumulative moment M_{cum} is distributed over the entire moment interval [0, $M_{\max}$]. The fraction $\Phi(M)$ of M_{cum} covered by a catalog that contains only events with moments between M_1 and M_2 is given by

$$\Phi(M) = \frac{1}{A}\int_{M_1}^{M_2} MP(M)dM \tag{14}$$

The constant A normalizes the integral and can be determined by integration from $M_1 = 0$ to $M_2 = M_{\max}$. Solution of (14) yields

$$\Phi(M) = \frac{M_2^{1-\beta} - M_1^{1-\beta}}{M_{\max}^{1-\beta}} \tag{15}$$

and the catalogued seismic moment M_{cat} contained in a catalog covering the moment interval [$M_{\min}$, $M_{\max}$] therefore is

$$M_{cat} = \left(1 - \frac{M_{\min}^{1-\beta}}{M_{\max}^{1-\beta}}\right) M_{cum} \tag{16}$$

In addition to $P(M)$ and $N(M)$, *Kagan* [2002a] also gives an equation that can be used to produce a list of n synthetic moments M_{sim}^i that are distributed according to equation (13):

$$M_{sim}^i = M_{\min}\left[X_i\left[1 - \left(\frac{M_{\max}}{M_{\min}}\right)^{-\beta}\right] + \left(\frac{M_{\max}}{M_{\min}}\right)^{-\beta}\right]^{-1/\beta} \tag{17}$$

where $X_i \in [0, 1]$ is the ith output number of a uniform random number generator. The number n must be chosen such that

$$M_{cat} = \sum_{i=1}^{n} M_{sim}^i \tag{18}$$

is approximately satisfied. Because of the stochastic nature of this process, exact equality will be achieved only in rare cases. In our implementation, the generation of new moment values is stopped when M_{cat} is exceeded, and in 50% of all cases, the last value is removed from the list. The average of all catalogs thus satisfies (18), but in individual runs, there is either a (usually small) excess or a lack of seismic moment.

2.3.4. Moment-Length Relation

[36] To produce a catalog of quake epicenters, we have to assign the seismic moment values constructed by equation (17) to points on faults of our fault catalog. This cannot be done purely by random decision, since the rupture area represented by the fault must be large enough to release the desired amount of seismic moment. We therefore need a relation between the surface length of rupture (since the surface length of faults is the only information we have) and the moment that can be released by a rupture of this length in order to determine the largest seismic moment a given fault can release.

[37] Empirical length-magnitude-relations for quakes on Earth have been derived by *Wells and Coppersmith* [1994], but these do of course imply properties of terrestrial tectonic regimes. Especially an implicit value of the seismogenic thickness would be grossly inconsistent with a determination of the Martian value from thermal evolution models. Instead of using the *Wells and Coppersmith* [1994] relations, we develop a model based on explicit physical and tectonic assumptions.

[38] Since we know only the fault length, we have to guess the rupture width. In the following, we utilize the rupture geometry used by *Schultz and Lin* [2001], *Schultz and Watters* [2001], and *Schultz* [2003], which is depicted in Figure 5. The rupture area is a dipping rectangle with dip angle δ, length L and width W. For faults that do not reach the maximum depth H, the thickness of the seismogenic lithosphere, we assume a constant aspect ratio $a = L/W$ as by *Schultz* [2003]. This yields a distinction between short and long faults: short faults reach only shallow depths $Z_F < H$ and by application of the aspect ratio, the rupture width is

$$W_{Short} = \frac{L}{a} \tag{19}$$

For long faults, the aspect ratio cannot be applied since the faulting depth Z_F cannot exceed H, and thus the rupture width is

$$W_{Long} = \frac{H}{\sin\delta} \tag{20}$$

For a fault of given length L we therefore assume that the width is given by

$$W = \min\left(W_{Long}, W_{Short}\right) \tag{21}$$

Table 1. Ranges of Numerical Values and Physical Units for All Model Parameters[a]

Parameter	Symbol	Value	Units
Planetary radius	R_P	3389.515	km
Seismogenic lithosphere thickness	H	40...150	km
Thrust fault dip angle	δ_T	25	degrees
Normal fault dip angle	δ_N	60	degrees
Rupture area aspect ratio	a	2...3	1
Lithospheric cooling rate	T	0.2...1.1	10^{-7} Ka^{-1}
Thermal expansion coefficient	α	2...3	10^{-5} K^{-1}
Shear modulus	μ	30...70	GPa
Poisson's ratio	ν	0.25	1
Static stress drop	$\Delta\sigma$	3...10	MPa
Seismic efficiency	η	0.5...1	1
Minimum seismic moment	$M_{\min}$	3.98×10^{10}	Nm
Maximum seismic moment	$M_{\max}$	$3.4 \times 10^{16} \ldots 3.4 \times 10^{20}$	Nm
Distribution slope	β	0.625	1/log(Nm)
Catalog time window	Δt	1	years
Maximum fault age	$t_{\max}$	0.5 or 5	Ga

The rectangular shape and aspect ratio a are assumed not only for the entire fault, but also for the individual rupture area A, which is then

$$A = LW \tag{22}$$

Finally, to obtain a moment-length relation, we have to determine the average slip $\overline{S}$.

[39] *Kanamori and Anderson* [1975] state that the static stress drop $\Delta\sigma$ of earthquakes is constant over a wide range of magnitudes. This is equivalent to the average slip on the rupture area depending only on rupture width W, but not on rupture length L. Since the publication of *Kanamori and Anderson*'s [1975] paper, there is a discussion (which we will not review here) if the static stress drop is really constant for all quake sizes, and what could be the underlying physics. *Bodin and Brune* [1996] conclude that the available data does not rule out one of the two models in question and the duration of the (still continuing [e.g., *Liu-Zeng et al.*, 2005]) discussion supports this conclusion. Since no clearly superior model is available, we decided to use the constant stress drop hypothesis to model the average slip.

[40] The static stress drop on normal and thrust faults is given by

$$\Delta\sigma = C\mu\frac{\overline{S}}{W} \tag{23}$$

[e.g., *Kanamori and Anderson*, 1975], where C is a geometry-dependent constant of order unity. *Starr* [1928] found that for dip slip faults, C is given by

$$C = \frac{4(\lambda+\mu)}{\pi(\lambda+2\mu)} \tag{24}$$

with λ being the Lamé-Parameter. Using the shear modulus μ and Poisson's ratio ν, the Lamé-Parameter can be expressed as

$$\lambda = \frac{2\mu\nu}{1-2\nu} \tag{25}$$

[e.g., *Stacey*, 1992]. By inserting (25) into (24), C becomes

$$C = \frac{2}{\pi}\frac{1}{1-\nu} \tag{26}$$

and with (23) this yields the average slip

$$\overline{S} = \frac{2\Delta\sigma W}{\pi\mu(1-\nu)} \tag{27}$$

Combination of equations (2), (22), and (27) yields the moment-length-relation

$$M_0(L) = \frac{2}{\pi}\frac{\Delta\sigma}{(1-\nu)}L\min\left(\frac{H}{\sin\delta}, \frac{L}{a}\right)^2 \tag{28}$$

A simulated quake with seismic moment M_{sim} may therefore be assigned to a fault of mapped length L only if $M_{sim} \leq M_0(L)$.

[41] Since numerical values for the moment-length relation depend on the model parameters, they will be shown in the results section.

2.4. Model Parameters

[42] Our seismicity model is defined by equations (9), (17), and (28). The model has a total of 16 input parameters which are summarized with their numerical ranges in Table 1. In the following, we discuss the ranges given in Table 1 for each parameter separately. Finally, we compose several end-member models of the Martian seismicity.

2.4.1. Planetary Radius

[43] Our computation of the seismogenic volume in equation (6) and of the strain rate in equation (7) is based on the assumption of a spherical planet. To obtain the correct volume, the radius of this sphere must be that of the volume-equivalent sphere of the reference ellipsoid. The half axes of the ellipsoid are given by a = 3398.627 km, b = 3393.760 km, and c = 3376.200 km [*Smith et al.*, 1999], and therefore the planetary radius we have to use here is R_P = 3389.515 km.

2.4.2. Seismogenic Lithosphere Thickness

[44] Several different approaches to determine the thickness of the seismogenic lithosphere are possible: (1) the depth extent of faults as determined from topography modeling, (2) the elastic lithosphere thickness as determined from gravity/topography ratios, and (3) the depth of isotherms as estimated by thermal evolution models all give different thicknesses. *Golombek et al.* [1992] assumed a faulting depth of 2.5 km for typical simple grabens. The faulting depth in the Amenthes Rupes region is 25–30 km [*Schultz and Watters*, 2001], the largest graben structures in Valles Marineris reach a depth of 60–75 km, whereas smaller ones are probably limited to 3–10 km [*Schultz and Lin*, 2001]. For the estimation of a global average, the greatest depths in Valles Marineris must probably be considered as outliers. Since all modeled faulting depths are valid for the time of faulting, they probably underestimate the faulting depth possible today. The upper limit of the Amenthes Rupes region therefore seems to be a good candidate for a global average of the seismogenic lithosphere thickness.

[45] The elastic lithosphere thickness as determined from gravity data shows a great variability. In isostatically compensated areas, it is generally zero, which does of course not imply that isostatically compensated material cannot be brittle. According to *Frey et al.* [1996], the isostatic compensation depth of Amazonian units not belonging to the Tharsis and Elysium uplifts is generally below 20 km, implying that the brittle lithosphere is even thinner. *Turcotte et al.* [2002] estimate the global average elastic thickness of 90 ± 10 km. *McGovern et al.* [2004] determine elastic thicknesses for many areas. For areas of Amazonian age, they give values between 2 km and 200 km. It must be taken into account that the elastic thickness values are valid not for today but for the time of loading, so the thickness relevant for today's seismicity might be different.

[46] If the seismogenic lithosphere thickness is derived from thermal evolution models, it is not a free parameter but closely connected to the volumetric expansion coefficient and the cooling rate. To obtain a physically meaningful model, it is important to choose these three values consistently.

[47] Several different isotherms are relevant as boundaries of the seismogenic layer, mainly those at temperatures of 573 K, 873 K, and 1073 K. The most ductile constituent of granitic crust, quartz, becomes plastic at a temperature of 573 K, which is why this isotherm is often identified with the bottom of the quake nucleation zone [*Scholz*, 1998]. Since the Martian crust is usually not thought to be granitic, but basaltic and andesitic [e.g., *Zuber*, 2001], *Phillips* [1991] uses the 1073 K isotherm, which is presumed to limit the maximum depth of oceanic intraplate quakes on Earth. However, it is not clear that it is really the 1073 K isotherm that limits the depth of oceanic intraplate seismicity. *Stein and Stein* [1996] restrict the maximum temperature at oceanic earthquake foci only to an interval, from 873 K to 1073 K, and *Abercombie and Ekström* [2001] claim that the maximum depth of brittle failure in oceanic crust is indeed limited by a temperature of ≈873 K, based on the hypocentral depths of earthquakes located on oceanic transform faults.

[48] *Phillips* [1991] and *Golombek* [2002] use the depth of the 1073 K isotherm as bottom of the seismogenic lithosphere and get a thickness of H = 150 km from thermal evolution modeling. *Schultz* [2003], on the other hand, identifies the 573 K isotherm with the faulting depth of H = 30 km determined by *Schultz and Watters* [2001].

[49] We use the thermal evolution model of *Schumacher and Breuer* [2006] to estimate the depth of all three isotherms in discussion. The 573 K isotherm is found at a depth of 41 km, the 873 K isotherm follows at a depth of 107 km, and the 1073 K isotherm is situated at a depth of 150 km (D. Breuer, personal communication, 2005). The depth of the 1073 K isotherm is identical to that used by *Phillips* [1991], although our thermal expansion coefficient was lower ($\alpha = 2 \times 10^{-5}\ K^{-1}$). The thermal evolution results do in fact not depend significantly upon the expansion coefficient.

[50] These three isothermal depths cover almost the entire range of faulting or isostatic compensation depths discussed above, and they are the only depth values that are valid for today. Additionally, they can be chosen fully consistent with the thermal contraction coefficient and the cooling rate. We therefore chose the depths of the 573 K and the 1073 K isotherms as end-members for the seismogenic lithosphere thickness.

2.4.3. Fault Dip Angle

[51] Several authors investigate the dip angles of faults on Mars, based on a modeling of the observed topography. Since normal faults usually dip much steeper than thrust faults, two parameters δ_N and δ_T for normal and thrust faults, respectively, have to be estimated for our model.

[52] *Watters and Robinson* [1999] find a dip angle of $\delta_T = 20°–35°$ with an optimum value of $\delta_T = 25°$ for the thrust faults of the Terra Cimmeria-Amenthes region. For Amenthes Rupes, this range is narrowed to $\delta_T = 24°–30°$ by *Watters et al.* [2000] or $\delta_T = 25°–30°$ by *Schultz and Watters* [2001]. *Watters* [2003] gives the same range and again uses $\delta_T = 25°$ as generalization.

[53] *Davis and Golombek* [1989] find dip angles of about $\delta_N = 60°$ for grabens in Noctis Labyrinthis, Valles Marineris, and Sacra Fossae, and consequently, *Golombek et al.* [1992] assume a $\delta_N = 60°$ dip for normal faults. *Schultz and Lin* [2001] find dip angles of $\delta_N = 40°–55°$ for normal faults in Valles Marineris and assume that small grabens may range from $\delta_N = 50°$ to $\delta_N = 65°$. *Wilkins et al.* [2002] find $\delta_N = 60°$ for normal faults and grabens on Tempe Terra.

[54] On the basis of these observations, we adopt a dip angle of $\delta_T = 25°$ for thrust faults and an angle of $\delta_N = 60°$ for normal faults.

2.4.4. Rupture Area Aspect Ratio

[55] *Nicol et al.* [1996] analyze slip distributions and the aftershock sequences of terrestrial faults and report rupture area aspect ratios that are typically between 1 and 3. *Schultz* [2003] uses end-member values of $a = 2$ and $a = 3$ in his analysis of the Amenthes Rupes seismotectonics. We adopt these two values for our end-members.

2.4.5. Lithospheric Cooling Rate

[56] Today's cooling rate of the lithosphere can be estimated from thermal evolution models only. The model used by *Phillips* [1991] resulted in a cooling rate of $\dot{T} = 1.1 \times 10^{-7}$ K yr^{-1}. As for the seismogenic lithosphere thickness, we use the model of *Schumacher and Breuer* [2006]. The cooling rate is determined from the temperature distribution in the lithosphere down to the depth of a predefined isotherm and therefore depends on the chosen isotherm. The uppermost part of the lithosphere, down to the depth of the 573 K

isotherm, cools at a rate of $\dot{T} = 0.2 \times 10^{-7}$ K yr^{-1}. Deeper portions cool slower, but the cooling rate changes only little in greater depths. If the depths of the 873 K and 1073 K isotherms are used, the cooling rate is $\dot{T} = 0.5 \times 10^{-7}$ K yr^{-1} in both cases (D. Breuer, personal communication, 2005). We use $\dot{T} = 0.2 \times 10^{-7}$ K yr^{-1} and $\dot{T} = 1.1 \times 10^{-7}$ K yr^{-1} as extreme cases.

2.4.6. Thermal Expansion Coefficient

[57] The coefficient of thermal expansion in the evolution model of *Schumacher and Breuer* [2006] is $\alpha = 2 \times 10^{-5}$ K^{-1}, whereas *Phillips* [1991] uses a higher value of $\alpha = 3 \times 10^{-5}$ K^{-1}. Both values are frequently found in the literature. However, the numerical results for cooling rate and isothermal depth do not depend significantly on α (D. Breuer, personal communication, 2005). In terms of thermodynamic consistency it is therefore not important which one we use. Since the annual cumulative moment is proportional to α, we use both to obtain end-member models.

2.4.7. Shear Modulus

[58] The seismic moment released by a given rupture is proportional to the shear modulus μ of the ruptured medium, and therefore the annual seismicity as function of the annual moment budget is also proportional to μ. In the Earth model PREM [*Dziewonski and Anderson*, 1981], the shear modulus at the surface is $\mu = 26.6$ GPa. The lithospheric maximum is reached below the base of the crust where $\mu = 68.2$ GPa.

[59] The values used in the literature on tectonic inversion of Martian topography essentially fall in the range given by PREM, but depend on the preferred type of crust and the depth range under consideration. *Schultz and Lin* [2001], in their modeling of Valles Marineris faults, use a Youngs modulus as low as $E = 10$ GPa, corresponding to $\mu = 4$ GPa in a Poisson solid. *Phillips* [1991] and *Zhong* [2002], on the other hand, use the much higher value of $\mu = 70$ GPa. Most authors assume a shear modulus in the range $\mu = 20-40$ GPa [*Schultz and Watters*, 2001; *Turcotte et al.*, 2002; *McGovern et al.*, 2002; *Schultz*, 2003; *Wilkins and Schultz*, 2003; *Grott et al.*, 2005].

[60] We adopt values of $\mu = 30$ GPa for the end-member model with many but weaker quakes and $\mu = 70$ GPa for the end-member with few but stronger quakes.

2.4.8. Poisson's Ratio in the Lithosphere

[61] We follow the common practice [*Schultz and Watters*, 2001; *Schultz and Lin*, 2001; *Wilkins and Schultz*, 2003; *Turcotte et al.*, 2002; *McGovern et al.*, 2002; *Grott et al.*, 2005] to assume that the Martian lithosphere is a Poisson solid with $\nu = 0.25$.

2.4.9. Static Stress Drop

[62] In theory, static stress drop is a fundamental parameter controlling the size of an earthquake. In the practical inversion of seismic data it turns out that it is remarkably difficult to determine. *Kanamori* [1994] lists five different methods to estimate the stress drop of a given quake. These methods use different types of data and represent different averages over the rupture area. Results that differ by a factor of 4 or 5 for the same quake are therefore not unusual [*Scholz*, 2003]. When *Kanamori and Anderson* [1975] first reported the phenomenon of constant stress drop, they estimated the typical stress drops of $\Delta\sigma = 3$ MPa for interplate quakes and $\Delta\sigma = 10$ MPa for intraplate quakes. This factor of about 3 between the two groups of quakes is generally agreed upon, but *Fujii and Matsu'ura* [2000] give $\Delta\sigma = 1.8$ MPa for interplate quakes and $\Delta\sigma = 3.1$ MPa for intraplate quakes, whereas *Shaw and Scholz* [2001] give $\Delta\sigma = 4$ MPa for interplate and $\Delta\sigma = 12$ MPa for intraplate quakes. The values of *Bodin and Brune* [1996] overlap both ranges, being $\Delta\sigma = 1 \ldots 3$ MPa at plate boundaries and $\Delta\sigma = 2.8-5$ MPa in plate interiors.

[63] *Goins et al.* [1981] determine stress drops for moonquakes and find a clear distinction between deep and shallow (HFT) moonquakes. The shallow moonquakes show stress drops that are generally above 10 MPa, with a maximum of 140 MPa for the strongest event. However, these high values do not necessarily indicate that stress drop on the moon is generally higher than on earth. Events with stress drops up to 200 MPa are also reported on Earth [*Kanamori*, 1994], and given the uncertainty in absolute stress drop determinations mentioned above, and given the small number of shallow moonquakes, the HFT quakes do not seem to constitute a fundamental difference between Earth and Moon.

[64] On Mars, we deal only with plate interior regions. On the basis of the above, we use end-member values of $\Delta\sigma = 3$ MPa and $\Delta\sigma = 10$ MPa.

2.4.10. Seismic Efficiency

[65] The cumulative seismic moment release is dominated by the moment of the largest quakes, and since large quakes are rare, it is difficult to determine the value η of seismic efficiency.

[66] The regional variability of η on Earth is quite large. For the USA, *Ward* [1998a] finds values that are essentially between $\eta = 0.025$ and $\eta = 0.86$, and the range for Europe is $\eta = 0.03$ K 0.71 [*Ward*, 1998b].

[67] Most of the seismic activity on Earth is of course due to plate tectonics, the seismic efficiency of which may be irrelevant for Martian tectonics. However, from the mentioned variability we conclude that the full range $0 \leq \eta \leq 1$ is possible. Seismic efficiency is thus considered to be a physical parameter we can use to produce high- and low-seismicity end-member models at will. We adopt values of $\eta = 1$ for high-seismicity models and $\eta = 0.5$ for low-seismicity models.

2.4.11. Maximum Seismic Moment

[68] The size of the greatest possible quake is difficult to estimate even if a long event record is available: one can never be sure that the greatest possible quake already occurred, and it is in fact likely that it did not.

[69] Using oceanic intraplate earthquakes as a guide, *Phillips* [1991] estimates the largest possible moment as $M_{\max} = 10^{20}$ Nm, whereas *Phillips and Grimm* [1991] assume the surface wave magnitude to be limited by $M_S = 6.0$ (corresponding to $M_{\max} = 2.5 \times 10^{18}$ Nm). *Golombek et al.* [1992] obtain an intermediate value of $M_{\max} = 10^{19.5}$ Nm as limit for the seismic moment.

[70] *Golombek* [1994] also takes continental intraplate quakes into consideration, since the strongest intraplate quakes occur at normal faults in continental crust. From these, he adopts the upper limit of $M_{\max} = 2 \times 10^{20}$ Nm for Martian thrust fault quakes.

[71] If we just feed the fault lengths of our catalog into our moment-length-relation and assume a stress drop of $\Delta\sigma = 10$ MPa, the largest possible moment we get is $M_0 \approx 4.8 \times 10^{23}$ Nm ($M_W = 9.7$). This is more than twice the moment release of the great Chile earthquake of 1960 ($\approx 2 \times 10^{23}$ Nm or $M_W = 9.4$ [*Kanamori and Anderson*,

Table 2. Model Parameters for Seismicity Models With Different Annual Moment Budgets ("Strong", "Medium", and "Weak"), Distributed Over "Few", "Medium," or "Many" Quakes[a]

	Units	STRONGFEW	STRONGMANY	MEDIUM	WEAKMANY	WEAKFEW
R_P	km	3389.515	3389.515	3389.515	3389.515	3389.515
H	km	150	150	107	40	40
δ_T	degrees	25	25	25	25	25
δ_N	degrees	60	60	60	60	60
a	1	2	3	2.5	3	2
$\dot{T}$	10^{-7} Ka^{-1}	1.1	1.1	0.5	0.2	0.2
α	10^{-5} K^{-1}	3	3	2	2	2
μ	GPa	70	70	40	30	30
ν	1	0.25	0.25	0.25	0.25	0.25
$\Delta\sigma$	MPa	10	3	5	3	10
η	1	1	1	1	0.5	0.5
$M_{\min}$	Nm	3.981×10^{10} ($M_W = 1$)	3.981×10^{10}	3.981×10^{10}	3.981×10^{10}	3.981×10^{10}
$M_{\max}$	Nm	3.36×10^{20}	3.42×10^{16}	2.41×10^{18}	3.42×10^{16}	3.37×10^{20}
β	1/log(Nm)	0.625	0.625	0.625	0.625	0.625
Δt	years	1	1	1	1	1
$t_{\max}$	Ga	5	5	5	5	5

1975]), the greatest quake observed on Earth by now. This value certainly overestimates the Martian $M_{\max}$ by far.

[72] In the years 1984–2004, the annual moment release of the Earth varied between 1.89×10^{21} Nm in 1988 and 4.3×10^{22} Nm in 2004, with a median of $\tilde{M}_{cum} \approx 2.8 \times 10^{21}$ Nm, according to the respective lists of the Harvard CMT project [*Dziewonski and Woodhouse*, 1983] (see also *Dziewonski et al.*, [1983] and annual updates). If we transfer the moment ratio

$$\frac{M_{Chile}}{\tilde{M}_{cum}} = 70.32 \tag{29}$$

between the Chile earthquake, which was close to the largest possible quake on Earth [*McGarr*, 1976], and the Earth's median annual release from Earth to Mars, our different models (see section 2.4.16) give a range $M_{\max} \approx 2.41 \times 10^{18} \ldots 3.36 \times 10^{20}$ Nm or $M_W = 6.2 \ldots 7.6$. We think that at least the upper value also overestimates the true $M_{\max}$.

[73] If we assume that the greatest possible quake on Mars is one which releases the annual cumulative moment within a single event, our different models give a range $M_{\max} \approx 3.42 \times 10^{16} \ldots 4.78 \times 10^{18}$ Nm or $M_W = 4.9 \ldots 6.4$. This assumption is somewhat arbitrary since there is nothing special about the period of one year, and it implies that strain can be accumulated only until the end of December. Since much longer accumulation times than one year are known to exist from seismic efficiency studies [*Ward*, 1998a], these values are likely to underestimate $M_{\max}$.

[74] We assume that the true value is bracketed by $M_{\max} \approx 3.4 \times 10^{16} \ldots 3.4 \times 10^{20}$ Nm or $M_W = 4.9 \ldots 7.6$. These brackets contain the previous estimates reported above and are very likely to contain the true value without giving an unnecessarily wide interval.

2.4.12. Minimum Seismic Moment

[75] Modeling of seismic wave amplitudes and the detection performance of seismic networks on Mars [*Mocquet*, 1999; *Lognonné et al.*, 2000] shows that 60% of all seismic events with a moment exceeding $M_0 = 10^{13}$ Nm ($M_W = 2.6$) can be detected by a four station seismic network if the instrumental noise level is 5×10^{-10} ms^{-2} Hz$^{-1/2}$ or less, which was indeed a design goal for the NetLander seismometer [*Lognonné et al.*, 2000], and if no crustal scattering occurs. Quakes of this size therefore have to be contained in any simulated catalog. Quakes with magnitudes below 1, on the other hand, are so numerous that it becomes difficult to handle the catalogs. We therefore set the lower moment threshold to $M_W = 1$, corresponding to $M_0 \approx 3.98 \times 10^{10}$ Nm, in all models.

2.4.13. The β Value

[76] According to equation (12), it is important to distinguish between the slope b of a magnitude-frequency distribution and slope β of a moment-frequency distribution.

[77] *Goins and Lazarewicz* [1979] assume a b value of 1 (corresponding to $\beta = 2/3$) for Mars. *Phillips* [1991] uses the slightly larger value $\beta = 0.67$, based on oceanic intraplate earthquakes, and *Golombek et al.* [1992] and *Golombek* [2002] use a smaller value of $\beta = 0.60$, also based on oceanic intraplate event data.

[78] In a series of papers, *Kagan* [1997, 1999, 2002a, 2002b] investigates the regional variations of β on Earth and finds that, except for quakes close to the Olivine-Perovskite- transition (660 km depth on Earth) and quakes close to mid-ocean ridges, the slope parameter is a universal constant with value $\beta \approx 0.60 \ldots 0.65$, where the interval width represents the statistical uncertainty. According to Kagan, all apparent regional variations of β are statistically not significant. This result is confirmed by *Godano and Pingue* [2000] who use the same event catalog as *Kagan* [1997, 1999] but with a different regionalization.

[79] Since the existence of an Olivine-Perovskite transition in the Martian mantle is doubtful [e.g., *Sohl and Spohn*, 1997; *Bertka and Fei*, 1998] and mid-ocean ridges are not present on the Martian surface, we adopt a slope of $\beta = 0.625$ (the middle of the interval given by *Kagan* [2002b]) for the moment-frequency distribution in all models.

2.4.14. Catalog Time Window

[80] This parameter defines the time range for which the cumulative seismic moment is computed and thus the time range covered by the quake catalog. We compute cumulative moment, moment-frequency distributions, recurrence rates and simulated epicenter maps for a time window of one Julian year (365.25 days of 24 hours).

2.4.15. Maximum Allowed Fault Age

[81] Considering the spatial distribution of quakes it must be asked if all visible faults are tectonically active or if a

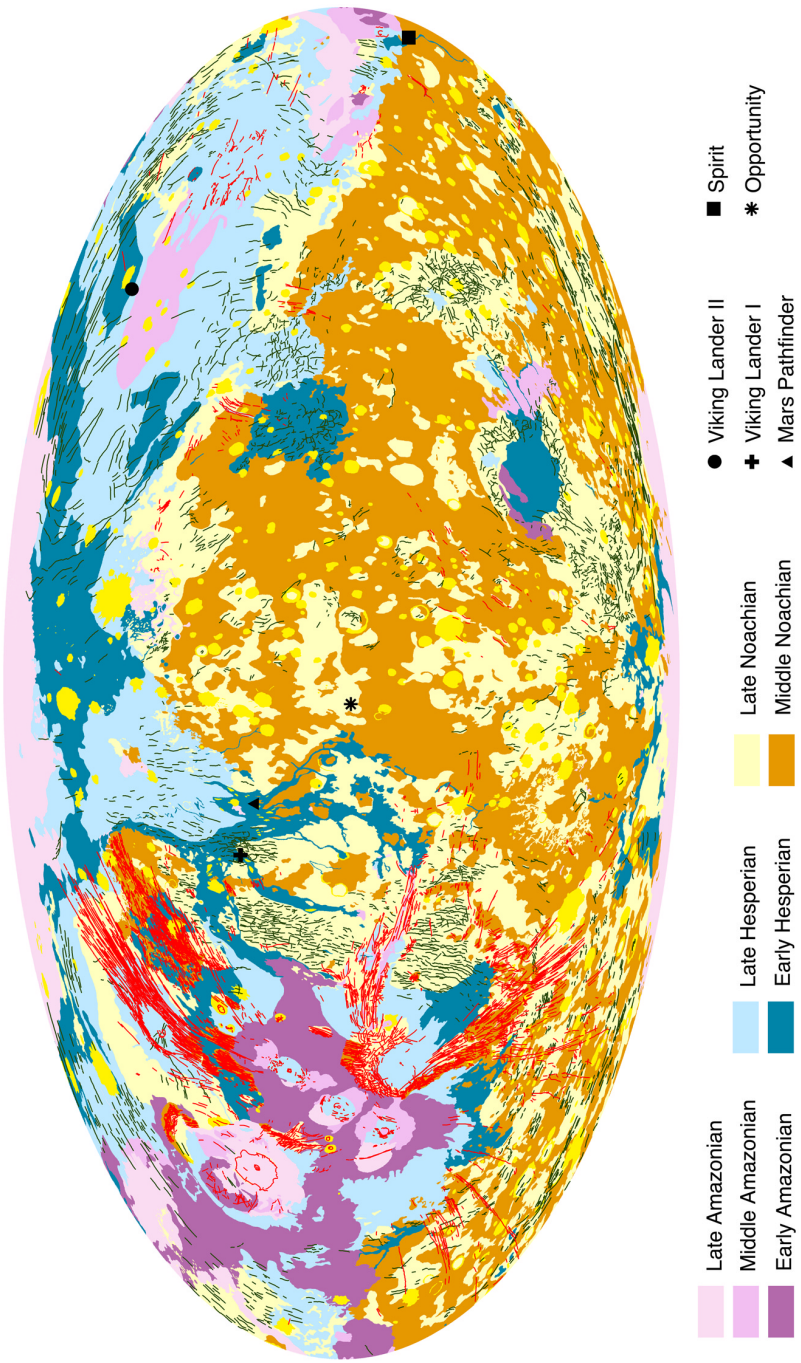

Figure 6. Extensional (red) and compressional (green) faults on a map of Mars surface ages. Surface colors denote the seven main epochs of Martian geology. Black symbols denote positions of successful lander missions. Map is in Mollweide projection.

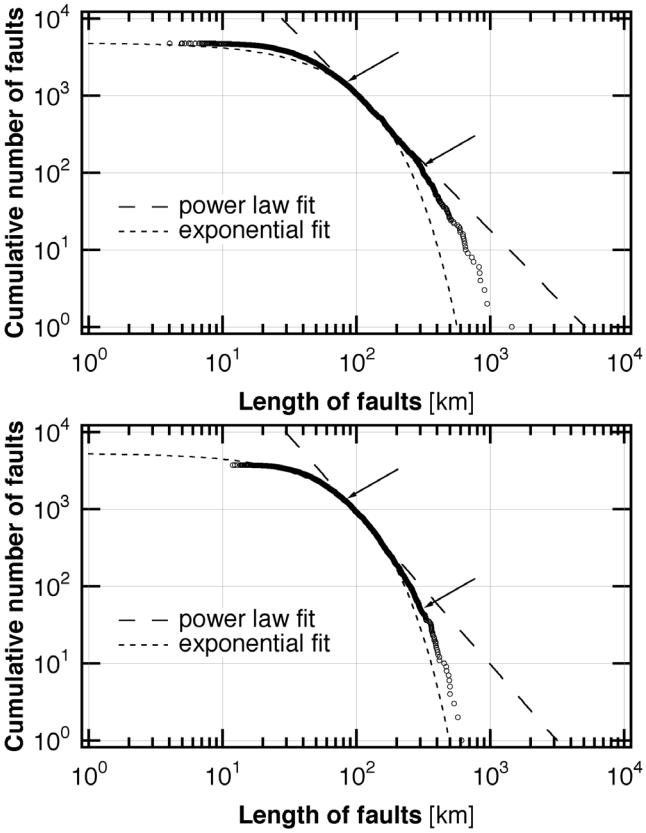

Figure 7. Log-log plot of cumulative frequencies of (top) extensional and (bottom) compressional fault lengths for the global, MOLA-based data set. A power law (see text for details) and, for comparison, an exponential function were fitted to the data between lengths of 80 and 300 km (arrows). The power law exponents are 1.77 and 1.97 for extensional and compressional faults, respectively.

healing process has deactivated some fraction of them. The only handle on possible fault deactivation we currently have is the age of the surface disturbed by the fault, which gives the maximum age of the last fault activity. As end-members of the spatial distribution we assume two cases: (1) all faults are seismically active today, yielding the broadest spatial distribution or (2) only faults in areas younger than t_{min} = 0.5 Ga are active, resulting in a concentration of seismicity in few relatively small areas.

2.4.16. Five Models

[82] From the parameter ranges discussed in the previous sections, we construct several end-member models: (1) STRONGFEW with a high seismic moment budget, distributed over few events, (2) STRONGMANY with a high seismic moment budget, distributed over many events, (3) MEDIUM with a medium seismic moment budget, distributed over a medium number of events, (4) WEAKFEW with a low seismic moment budget, distributed over few events, and (5) WEAKMANY with a low seismic moment budget, distributed over many events.

[83] The cumulative moment is controlled by parameters η, μ, α, $\dot{T}$, Δt, and H (see Table 1), but static stress drop $\Delta\sigma$ and maximum moment M_{max} give handles on the number of events over which this moment is distributed. The FEW and MANY variants therefore differ in $\Delta\sigma$ and M_{max}. The actual input parameters of the five models are summarized in Table 2.

3. Results

3.1. Fault Catalogue

[84] We collected a total set of 3737 thrust faults and 4764 normal faults, ranging from lengths between 4 and 1445 km, with a total length of all faults of approximately 680,000 km (Figure 2). Using the geologic map, each fault section was assigned to a geologic region and a specific surface age (Figure 6).

[85] The distribution pattern of faults (Figure 2) and basic statistical data appear very much like those of previous studies. The size-frequency plot (Figure 7) shows a characteristic trisegment shape [*Mansfield and Cartwright*, 2001], affected by sampling biases at the smaller and the larger end of the population. The flattening of the curve toward lower fault lengths ($< \sim$80 km) probably reflects the resolution limit of the data set, and is, therefore a censoring artifact [e.g., *Yielding et al.*, 1992; *Kim and Sanderson*, 2005]. Although *Walsh and Watterson* [1992] have ascribed such a flattening to a natural property of the fault population, we do not favor this explanation in the case of the global, MOLA-based fault set, since resolution is clearly a limiting factor here. At large fault lengths ($> \sim$300 km), the curve becomes steeper. This effect has been described as a systematic result of low-topology sampling in a two-dimensional sampling window [*Marrett*, 1996]. Since we use a global data set (i.e., no windowing), this effect should not affect our data. More probable, postfaulting geologic processes might have modified the statistics of our fault size distribution [*Schultz and Fori*, 1996].

[86] The size-frequency distribution of fault populations is often described by a power law [e.g., *Marrett and Allmendinger*, 1992; *Marrett*, 1996; *Yielding et al.*, 1996; *Schlische et al.*, 1996] of the form:

$$N(L) = aL^{-C} \tag{29}$$

where $N(L)$ is the cumulative number of faults greater than or equal to length L, a is a parameter related to the size of the sample, and $-C$ is the power law exponent. We fitted the power law function only to faults within the range of 80–300 km, thus avoiding the effects of biased fault statistics (Figure 7). The results yield power law exponents of $\sim$1.97 for compressional faults and $\sim$1.77 for extensional faults. These values fall well within the range of power law exponents found for faulting on Earth [*Yielding et al.*, 1996; *Mansfield and Cartwright*, 2001], as well as for the Valles Marineris and Tempe Terra extensional provinces on Mars [*Schultz and Fori*, 1996; *Schultz*, 2000b; *Wilkins et al.*, 2002]. We expect that the power law exponents for our fault sets would decrease if linkage of fault segments were considered [*Schultz*, 2000b]. For comparison, we also fitted an exponential function to our data set, which has also been suggested to represent fault populations [e.g., *Gupta and Scholz*, 2000; see also *Ackermann et al.*, 2001] and has the form

$$N(L) = ae^{-cL} \tag{30}$$

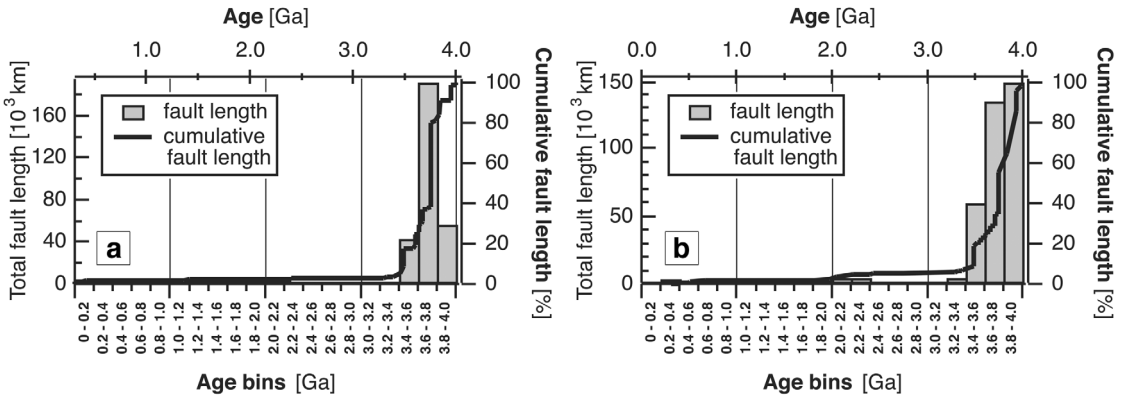

Figure 8. Absolute fault length production and relative cumulative fault length as function of age: (a) thrust faults and (b) normal faults.

We obtain values of c = 0.0173 and c = 0.015 for contractional and extensional faults, respectively.

[87] Although most of the faults were produced in the upper Noachian and Hesperian ages, when volcanic resurfacing reached its maximum [*Nimmo and Tanaka*, 2005] (Figure 8), no clear time-dependent preference for the production of longer or shorter faults is observed (Figure 9). The size-frequency relation therefore seems to be constant throughout time.

3.2. Seismicity

[88] The strain rates resulting from the parameters given in Table 2 are between $\approx 1.2 \times 10^{-20}$ s^{-1} or 0.004% strain in 100 Ma for the WEAK models and $\approx 1 \times 10^{-19}$ s^{-1} or

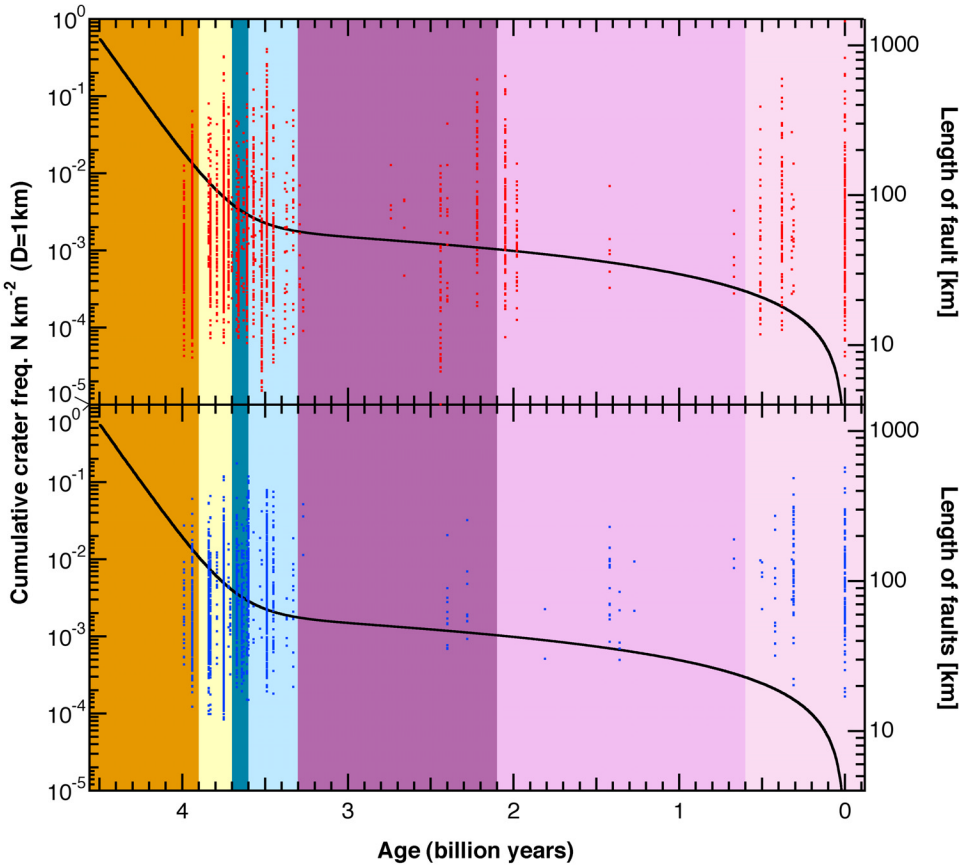

Figure 9. Lengths of faults versus fault age: The length of the individual faults plotted as function of model age. (top) Extensional faults (red dots) and (bottom) compressional faults (blue dots). Faults with age 0 are in undated terrains. Cumulative crater frequency is given for comparison. Background colors correspond to colors in Figure 6.

Table 3. Cumulative Seismic Moment of Our Models Together With Earthquake Recurrence Times

Magnitude	Moment	STRONGFEW	STRONGMANY	MEDIUM	WEAKMANY	WEAKFEW
M_{cum}		4.78×10^{18} Nm	4.78×10^{18} Nm	5.99×10^{17} Nm	3.42×10^{16} Nm	3.42×10^{16} Nm
$M_W \geq 1$	$M_0 \geq 4 \times 10^{10}$ Nm	38 min	72 s	48.5 min	2.5 h	3.9 d
2	1.3×10^{12} Nm	5.5 h	10.5 min	7 h	21.9 h	33.5 d
3	4×10^{13} Nm	1.9 d	1.5 h	2.5 d	7.9 d	290 d
4	1.3×10^{15} Nm	17.1 d	13.1 h	21.8 d	68.5 d	6.7 years
5	4×10^{16} Nm	148 d	-	189 d	-	50 years
6	1.3×10^{18} Nm	3.6 years	-	4.5 years	-	516 years
7	4×10^{19} Nm	30.3 years	-	-	-	~4500 years
7.6	3.2×10^{20} Nm	115 years	-	-	-	~17000 years

0.033% strain in 100 Ma for the STRONG models. The WEAK models thus comply with the estimate of Hesperian strain by *Hauck et al.* [2003], whereas the STRONG models predict a significantly higher strain. This suggests that the strain rate remained constant for a long time, or even increased.

[89] The cumulative seismic moment of our models are listed in Table 3, together with earthquake recurrence times. The annual moment budget of the STRONG models is about 8 times the budget of the MEDIUM model and about 140 times the budget of the WEAK models. The differences in seismogenic lithosphere thickness, cooling rate and shear modulus account for a factor 5.4 in the STRONG/MEDIUM ratio and a factor 48 in the STRONG/WEAK ratio. Besides the uncertainty in the seismic efficiency, these three quantities are thus the most important factors for the determination of the annual cumulative moment.

[90] The moment-frequency distributions corresponding to the recurrence times of Table 3 are shown for all models in Figure 10, which also compares them with the models of *Phillips* [1991], *Golombek et al.* [1992], and *Golombek* [2002], as described in section 1. Additionally, the moment-frequency relation for Earth, as derived from the catalog of the Harvard CMT project for the years 1984–2004 [*Dziewonski and Woodhouse*, 1983] (see also *Dziewonski et al.*, [1983], and annual updates) is shown in Figure 10. Our models essentially cover the range defined by the previous estimates. This is not too surprising, since some important parameters are identical, but our models give a physical justification especially for the lower bound of that range: Via the choice of the 300°C isotherm as bottom of the seismogenic lithosphere, the WEAK models are based on the assumption of a granitic crust, which is not present on Mars. A comparison of the isothermal depths of the different models thus shows that the WEAK models underestimate the seismic moment budget by a factor of about 2.5 and therefore give a hard lower bound for the budget.

[91] Most interesting for the determination of deep interior structure of Mars is the number of globally detectable quakes. If the threshold for global detection is roughly given by $M_W \geq 3$, then the WEAKFEW model predicts one such event all 290 days, whereas the STRONGMANY model

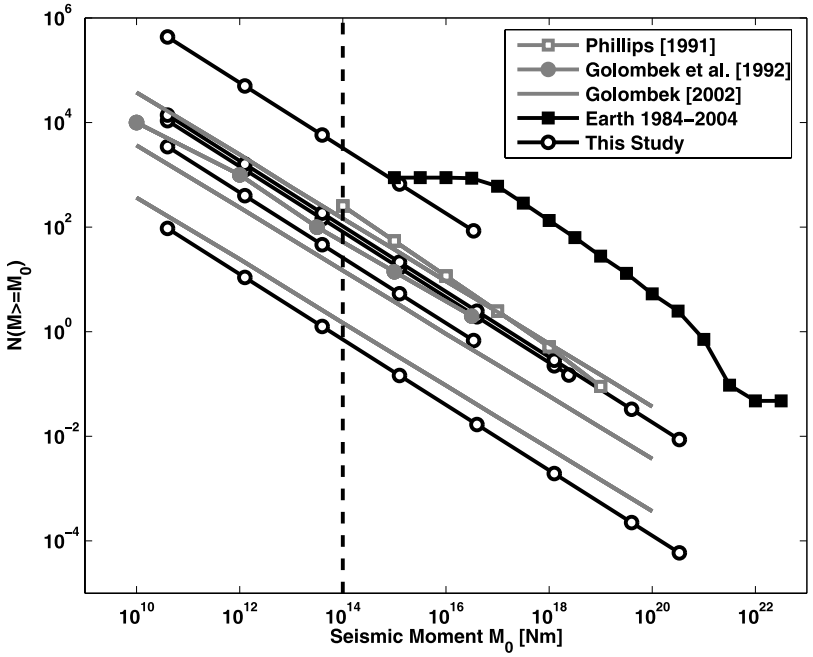

Figure 10. Moment-frequency-relation: comparison between previous studies, our models, and the annual moment release of Earth (Harvard CMT). Our models are, from top to bottom: STRONGMANY, STRONGFEW, MEDIUM, WEAKMANY, WEAKFEW, plotted in the moment ranges defined in Table 2. The vertical line denotes the threshold of global detectability by a low-noise four-station network [*Mocquet*, 1999].

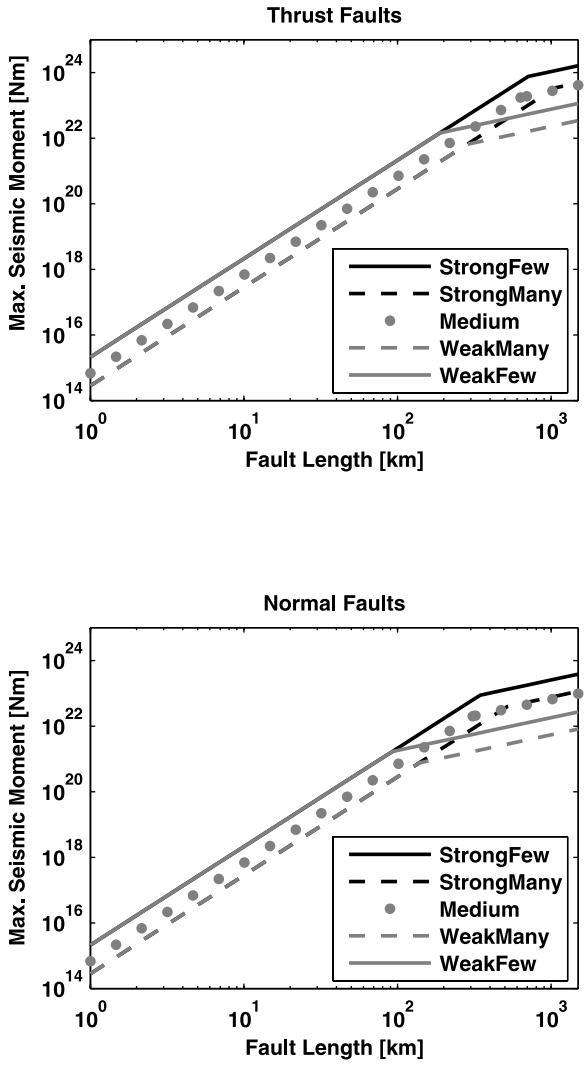

Figure 11. Moment-length relation: The greatest seismic moment a fault of given length can release for (top) thrust faults and (bottom) normal faults, shown for our five models. The kink corresponds to the length at which the fault reaches the bottom of the seismogenic layer.

offers an impressing number of 16 globally detectable events per day. Unfortunately, the large number of events in the STRONGMANY model is due to the size limitation of quakes; following this model, there will be no really big quakes. The MEDIUM and STRONGFEW models are more promising in this respect. This shows that, considering the number of quakes, there is an important trade off between cumulative seismic moment and the maximum possible quake size. This trade off can be resolved only by observation of a quake so big that a small $M_{\max}$ value can be ruled out – and thus by a sufficiently long mission life time.

[92] In order to distribute the randomly generated seismic moments resulting from equation (17), we relate the length of a fault to the largest seismic moment that can be released on that fault by equation (28), as depicted in Figure 11. This relation must be evaluated for each of our models separately, since it depends on several model parameters. For the longest faults, the maximum possible moment differs by about one decade between our models. As Figure 11 shows, even the shortest of our faults ($\sim$ 4 km), can release a quake with moment of about 1.8×10^{16} Nm ($M_W = 4.8$), which is large enough for global detection even in the case of strong crustal scattering [*Mocquet*, 1999].

[93] Besides the necessity that a fault must be long enough to produce the desired moment, we assume that quakes occur with uniform probability on all faults. For a quake small enough to occur on any of our faults (i.e., $M_W \leq 4.8$, see above), the probability that our model assigns it to a certain area is therefore given by the density of faults (cumulative fault length per area) in that area. Figure 12 shows a map of the spatial probability distribution for the occurrence of small quakes in our models, assuming that all faults are seismically active today (upper map) or only those faults in areas with surface age less than 500 Ma are active (lower map). For larger quakes, this probability must be modified, since not all faults are possible as source. However, since large quakes are rare and most of our faults are long enough for magnitude 6.5 quakes, the small quakes probability distribution is a good approximation to the probability of having a quake of any possible size.

[94] In the case of all faults assumed to be active, quake probability is highest on the Tharsis bulge, with local extrema on a few areas, namely Acheron, Ulysses, and Claritas Fossae, Valles Marineris, Alba Patera with its vast wristwatch fault system, and Tempe Terra. Somewhat isolated spots of increased probability (or fault density) are Hesperia Planum and Malea Planum.

[95] If only the youngest faults (surface age $\leq$ 500 Ma) are considered to be active, the situation changes dramatically, since most of the Martian surface is much older. Alba Patera, Claritas Fossae and Hesperia Planum do not play a role any longer, and only a small fraction of Acheron Fossae is allowed to bear epicenters in this case. The assigned seismicity of Arsia and Pavonis Mons increases, but Ascraeus Mons is also assumed to be aseismic now. Several isolated spots in the northern plains, on Elysium Planitia, as well as Terra Cimmeria, on the other hand, become local centers of seismic activity in this model.

[96] To assign the generated seismic moment lists to epicentral coordinates, we resample the faults to a uniform sample distance of about 2.5 km, yielding a total of 284,234 samples. For each of our model parameter sets, we generate a random list of seismic moments corresponding to the seismic moment release of one Julian Year as described in section 2. For the WEAK and MEDIUM models, the actual moment-frequency distribution of such a 1-year run depends very much on the unlikely presence of a large quake in the list. For the generation of epicenter catalogs, we chose runs such that their moment-frequency distribution is close to the long-term average as shown in Figure 10. The resulting epicenter distributions are shown in Figures 13, 14, and 15 for the WEAK, MEDIUM, and STRONG models, respectively.

[97] We show two versions of the MEDIUM model: One in which all faults are assumed to be seismically active (Figure 14, top), and one in which only faults are considered that cut surfaces younger than 500 Ma, assuming that some fault healing process deactivated the older ones (Figure 14, bottom). Both versions show exactly the same list of seismic moments, only the epicentral coordinates are different. For the STRONGMANY model, we show only the events with moment magnitude larger than 1. Since the number of weaker

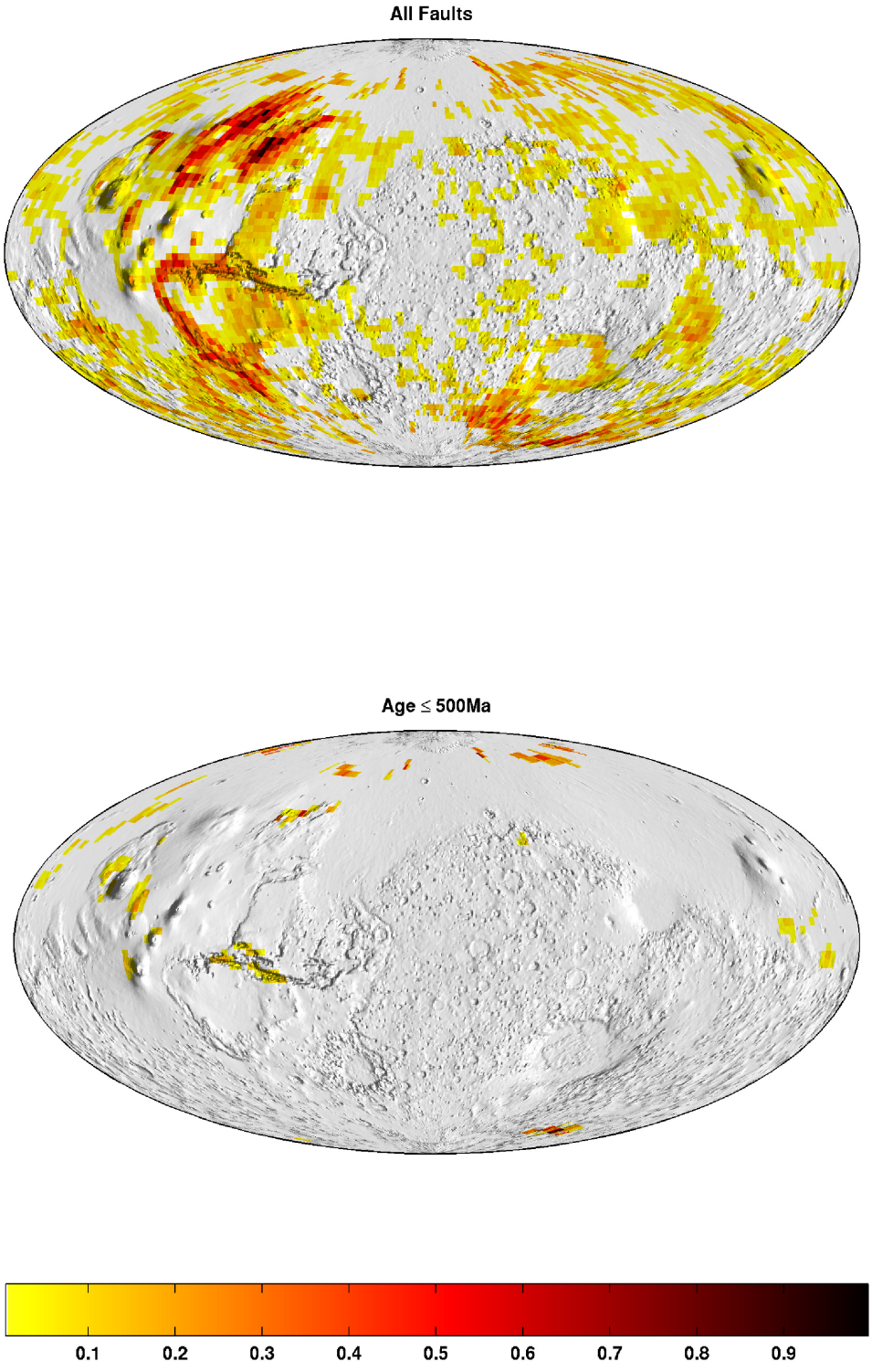

Figure 12. Probability that a small ($M_W \leq 4.8$) quake is assigned to 1 km^2 of surface, plotted on a 2.5° × 2.5° grid. (top) All faults considered, normalized to maximum by factor 4.88×10^{-7}. (bottom) Only faults cutting areas with surface age ≤500 Ma considered, normalized to maximum by factor 1.15×10^{-5}. Map is in Hammer's equal-area projection, centered on 0°N0°E, topography based on MOLA.

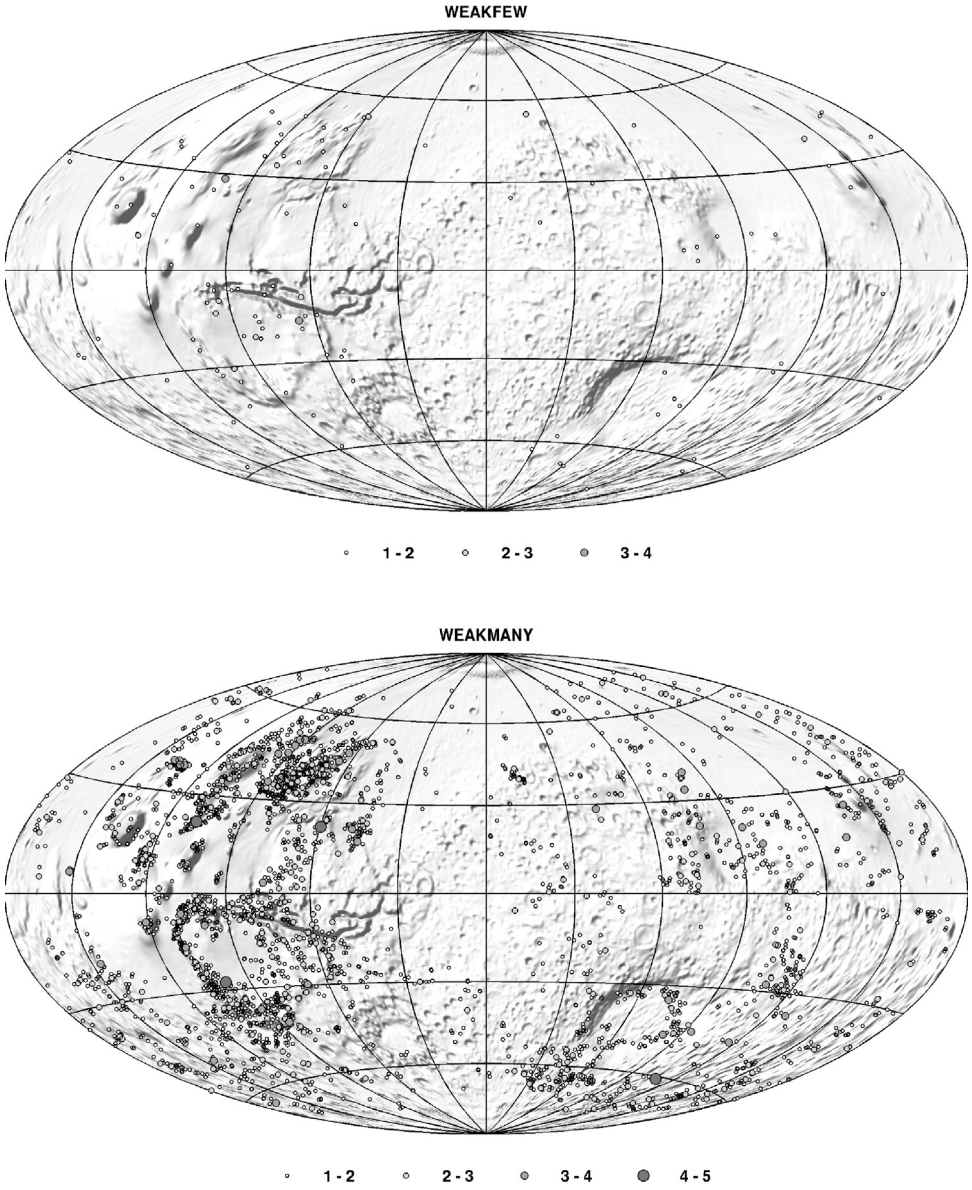

Figure 13. Example epicenter distribution for a 1-year run of the WEAK models. (top) WEAKFEW, with a total of 114 events. (bottom) WEAKMANY, with a total of 3467 events. Symbol size and shade denote moment magnitude. Map is as in Figure 12.

events is about 1.3 times the number of fault samples, the small events would just delineate all faults. From the MEDIUM and STRONG models we can expect that the main centers of seismicity become visible in epicenter maps after a few years of mission life time, if events with $M_W > 3$ are globally detectable. In case of the WEAK models, a longer registration time would be necessary, but the WEAKMANY model also promises a distribution of $M_W > 3$ events that may allow for a sounding of the Martian mantle.

4. Discussion

4.1. Tectonic Fault Catalog

[98] We have compiled a new catalog of tectonic faults on Mars. While our data set certainly lacks the detail in local areas, we expect that our global inventory is more homogeneous than the ones produced in previous studies. Our data set was collected from a uniform base map. Also, as we work under the "controlled illumination conditions" of the artificially shaded digital terrain model, we avoid sampling bias, e.g., the effect that faults of certain orientations are overrepresented or underrepresented. Hence the data are particularly suited for global statistics, e.g., for studies of spatial patterns of faults systems, fault length statistics, and correlations of surface faults with age.

[99] Admittedly, the age assignments on the basis of the geologic map are very crude, as the surface ages for some areas on Mars, with analyses based on old Viking Orbiter images, are poorly known. Fortunately, with the availability of new high-resolution image data from the Mars Global Surveyor, Mars Odyssey, and Mars Express missions, an update of the geologic map is on its way. First analyses by

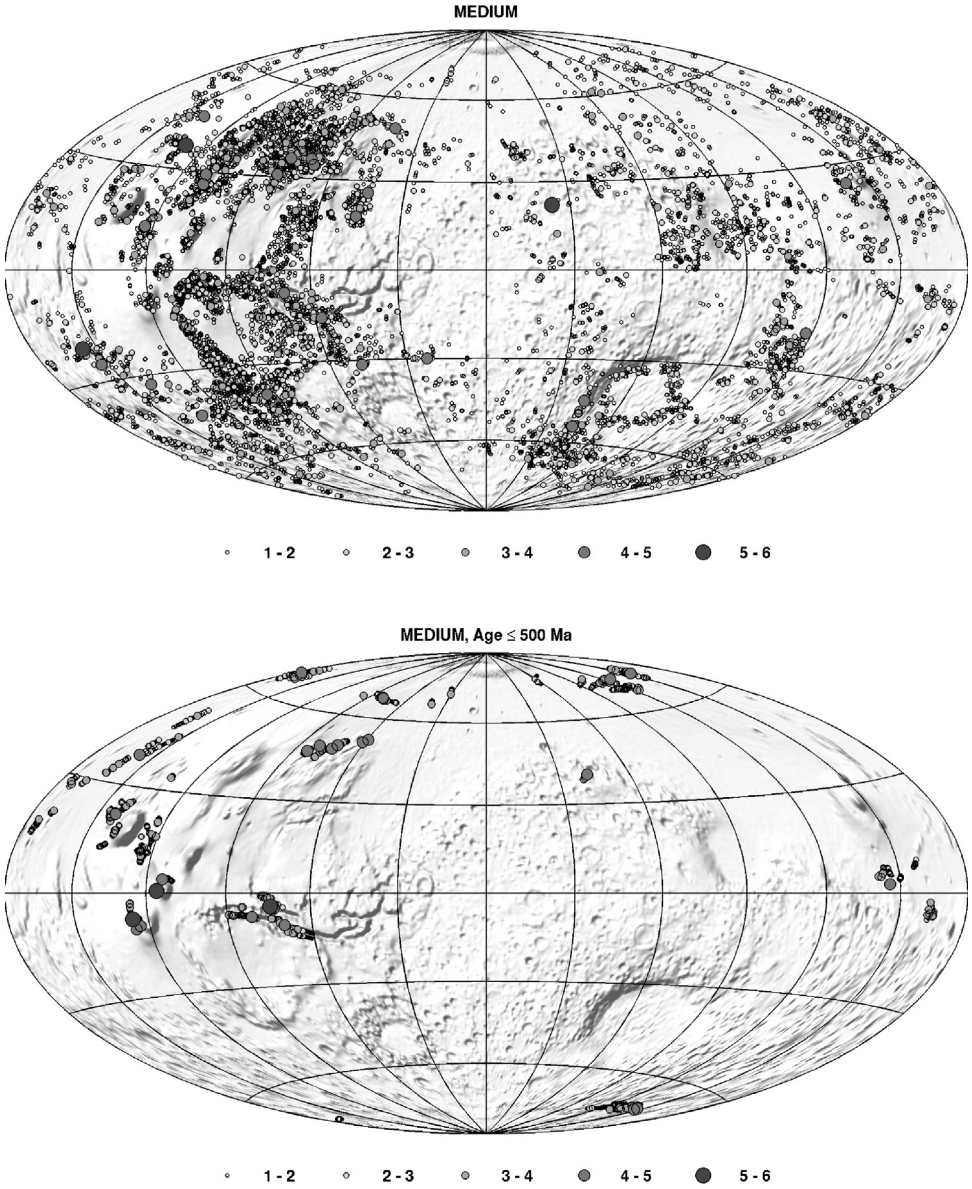

Figure 14. Example epicenter distribution for a 1-year run of the MEDIUM model. (top) All faults active. (bottom) Only faults on surfaces younger than 500 Ma active. Both versions contain 11,129 events with the same magnitude-frequency distribution. Symbol size and shade denote moment magnitude. Map is as in Figure 12.

e.g., *Tanaka et al.* [2003] seem to indicate that age assignments for some areas on Mars may differ substantially from what is believed today.

4.2. Seismicity Simulation

[100] In our simulation, we assume that seismic events occur on existing and visible surface faults only. Considering that highly fractured areas are probably less resistant against a globally uniform tectonic stress, a direct correlation of seismicity with the prevalence of faulting seems reasonable: Although the faults in our catalogue were created by other processes than global contraction, fractured rock is weaker than unfractured rock and will fail first under stress of any cause. The model is in accordance with the stick-slip model for crustal quakes on Earth, according to which most earthquakes occur on existing faults. This simplification seems also justified, because even the youngest tectonic features on Mars appear to be several million years old, i.e., new features have not been created for several millions of years. However, there may be additional sources of seismicity that are not modeled here. The retreat of the Magma chamber under Alba Patera, responsible for the creation of the characteristic wristwatch fault system [*Cailleau et al.*, 2003] has obviously been an important source of seismicity in the past. Similar processes may still be going on. Also, stresses associated with the known gravity anomalies, e.g., at Argyre or Isidis [*Zuber et al.*, 2000], may be responsible for locally increased seismic activity not accounted for in the energy budget of global thermal contraction. Meteoroid impacts are probably also an important source of seismic waves on Mars [*Davis*, 1993].

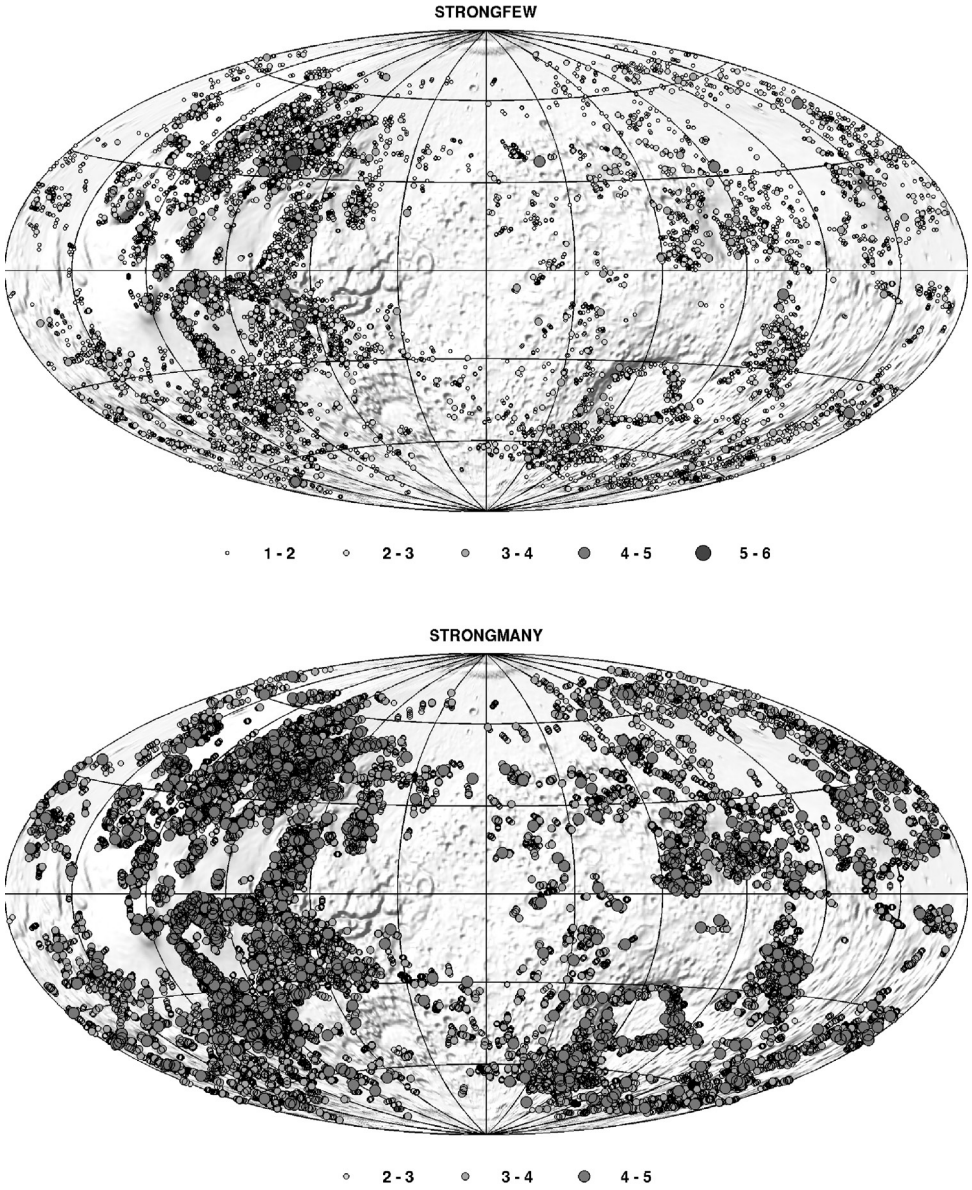

Figure 15. Example epicenter distribution for a 1-year run of the STRONG models. (top) STRONGFEW with a total of 13,641 events. (bottom) STRONGMANY with a total of 436,487 events (386,174 events with $1 \leq M_W \leq 2$ not shown). Symbol size and shade denote moment magnitude. Map is as in Figure 12.

[101] Certain Martian volcanoes (some of which were probably active in the recent past [*Neukum et al.*, 2004]) may still produce volcanic tremor not associated with visible surface faulting. Current volcanic activity on Tharsis, for example, would result in a locally increased seismic activity. However, as Figure 12 shows, an increased number of epicenters on Tharsis does not necessarily prove volcanic activity, since we expect an increased seismicity anyways, simply because of the higher fault density. To prove volcanic activity, the concentration of quakes must be higher than expected from fault density, or events must be identified as volcanic tremor by other criteria.

[102] Assuming that all points of all faults are equally probable as earthquake epicenter means to assume that the stress on all these points is the same. This is certainly an oversimplification, since the existence of faults modifies the local stress field. However, an accurate determination of the differential stress produced by the presence of the observed faults would need a separate study, encompassing a numerical simulation of the entire fault population. The actual stress field in the Martian lithosphere additionally depends on its seismic history and is even more difficult to determine. The assumption of uniform stress is the best we can currently do.

[103] We treat all faults as isolated individuals, although in areas of dense faulting, a mechanical linkage between neighboring faults is likely. This is discussed, e.g., by *Wilkins et al.* [2002] for the case of Tempe Terra: Two linked short faults together can release a seismic moment higher than the largest moment each of the individual faults can release. However, most of the faults in our catalog are

long enough even for the largest events in our quake catalogs, so that we do not expect a significant modification of the quake probability (Figure 12) from fault linkage.

[104] We also do not expect significant modifications from the fact that we map only surface faults visible in the 1-km MOLA topography we used. There are almost certainly invisible blind faults as well as faults much shorter than one kilometer and therefore below our resolution threshold. However, it is unlikely that the spatial density of invisible faults deviates significantly from the spatial density of our catalog. We do not expect, for example, that Arabia Terra, which is essentially aseismic in our models, turns out to be an important center of seismic activity because of blind faults. Considering the simulation of epicenter maps, the observed fault density is the only means to distribute epicenters in a tectonically meaningful way.

[105] The used 1km MOLA DTM often does not allow to distinguish between the two faults delimiting a graben, so many grabens are mapped as single normal faults. Therefore number of quakes in grabens is underestimated in many cases, for example in the extensional regions of Tharsis. Clearly, seismicity models in the Tharsis area (identified as the most prominent center of seismicity by our models) would benefit from an improved mapping at higher resolution.

[106] The seismicity models critically depend on the ages of the geologic units, many of which are uncertain. However, even if the surface ages of all geologic units were perfectly known, it is difficult to make a prediction on the today's seismicity on this basis alone. As a fault may have formed any time after the emplacement of the geologic unit, the ages of the units represent maxima of the fault ages only. It may well happen that young and active faults are located on old geologic units. Additionally, it is unlikely that the deformation of the southern hemisphere is seismically released by faults in the northern lowlands as required by the distribution of "young" faults shown in Figure 14. It will be useful to consider fault systems instead of individual faults. Utopia Planitia may serve as an example: some of the faults on the rim of Utopia are located on lava emplacements considered to be the youngest on Mars [*Neukum et al.*, 2004], whereas most of the surface of Utopia is of Hesperian age. Consequently, an epicenter distribution based on the youngest units (as in Figure 14, bottom) predicts high seismic activity concentrated on a few faults. However, these few faults are part of a large contiguous regional system. It is perhaps reasonable to assume that all these faults, regardless of the surface units on which they are located, are equally active. Following this reasoning, all of Utopia may represent a major center of seismic activity today. For the near future, we intend to revise the criteria for fault activity with respect to common origins in fault systems. We also plan to carry out a careful inspection of individual fault systems using additional data, e.g., the reconstruction of fault sequences and measurements of local cratering ages in high-resolution images could provide clues on their current activity. High-quality image data from the recent missions to Mars, Mars Global Surveyor and Mars Express, is in hand to address these issues.

5. Conclusion

[107] We present a new global catalog of Mars surface faults, comprising more than 8000 thrust and normal faults. The catalog is based on the MOLA terrain model and provides a representative and unbiased data set. While the catalog was specifically compiled to derive a working model for the seismic environment of Mars, we hope that it may be useful for a variety of geoscientific applications in the wider context of global Mars tectonics.

[108] We have also presented two spatial a priori probability distributions of quake occurrence and five different moment-frequency distributions for Martian seismicity, computed for competing basic assumptions and simulation parameters. Our "working model" of the Martian quake distribution is intended to be a tool to assess the science performance of planned seismological experiments. It incorporates many recent findings about Martian thermal evolution and tectonic features that were not available when previous estimates of Martian seismicity were published. However, this paper also demonstrates that any model of Mars seismicity cannot be unique, considering current knowledge. After all, it is our poor knowledge why we want to take seismometers to Mars! A comparison of future seismic data with the predicted seismicity maps of this study will help to identify deficiencies in our understanding of the dynamics of Mars and perhaps also Earth. This study convinces us that seismic experiments on future missions to Mars may be highly rewarding.

[109] The fault catalog as well as the epicenter lists used in Figures 13, 14, and 15 are available from the authors on request.

[110] **Acknowledgments.** This work was supported by the Deutsche Forschungsgemeinschaft contract SP219/19-2 within the Priority Programme "Mars and the Terrestrial Planets" and the European Community's Improving Human Potential Program under contract RTN2-2001-00414, MAGE. We thank our colleagues S. Ferrachat, V. Belleguic, and M. Grott for helpful discussions and D. Breuer for providing the cooling rates and isothermal depths. B. Endrun of RU Bochum dug up some of the older literature. We also thank P. Lognonné, R. Schultz, M. Golombek and anonymous reviewers for helpful and constructive comments, and AGU editors E. Calais and J. Moses for a smooth transition from GRL to JGR.

References

Abercombie, R. E., and G. Ekström (2001), Earthquake slip on oceanic transform faults, *Nature*, *410*, 74–77.

Ackermann, R. V., R. W. Schlische, and M. O. Withjack (2001), The geometric and statistical evolution of normal fault systems: An experimental study of the effects of mechanical layer thickness on scaling laws, *J. Struct. Geol.*, *23*, 1803–1819.

Anderson, D. L., R. L. Kovach, G. Latham, F. Press, M. N. Toksöz, and G. Sutton (1972), Seismic investigations: The Viking Mars Lander, *Icarus*, *16*, 205–216.

Anderson, D. L., W. F. Miller, G. V. Latham, Y. Nakamura, M. N. Toksöz, A. M. Dainty, F. K. Duennebier, A. R. Lazarewicz, R. L. Kovach, and T. C. D. Knight (1977), Seismology on Mars, *J. Geophys. Res.*, *82*, 4524–4546.

Anderson, R. C., J. M. Dohm, M. P. Golombek, A. F. C. Haldebamm, B. J. Franklin, K. L. Tanaka, J. Lias, and B. Brian (2001), Primary centers and secondary concentrations of tectonic activity through time in the western hemisphere of Mars, *J. Geophys. Res.*, *106*, 20,563–20,586.

Anderson, R. C., J. M. Dohm, A. F. C. Haldemann, T. M. Hare, and V. R. Baker (2004), Tectonic histories between Alba Patera and Syria Planum, Mars, *Icarus*, *171*, 31–38.

Anguita, F., A.-F. Farelo, V. López, C. Mas, M.-J. Muñoz-Espadas, A. Márquez, and J. Ruiz (2001), Tharsis Dome, Mars: New evidence for Noachian-Hesperian thick-skin and Amazonian thin-skin tectonics, *J. Geophys. Res.*, *106*, 7577–7589.

Artita, K. S., and R. A. Schultz (2005), Significance of deformation band-like strike-slip faults on Mars, *Lunar Planet. Sci., XXXVI* [CD-ROM], Abstract 2225.

Banerdt, W. B., M. P. Golombek, and K. L. Tanaka (1992), Stress and tectonics on Mars, in *Mars*, edited by H. H. Kieffer et al., pp. 249–297, Univ. of Ariz. Press, Tucson.

Bertka, C. M., and Y. Fei (1998), Implications of Mars Pathfinder data for the accretion history of the terrestrial planets, *Science*, *182*, 1838–1840.

Bodin, P., and J. N. Brune (1996), On the scaling of slip with rupture length for shallow strike-slip earthquakes: Quasi-static models and dynamic rupture propagation, *Bull. Seismol. Soc. Am.*, *86*, 1292–1299.

Bormann, P., M. Baumbach, G. Bock, H. Grosser, G. L. Choy, and J. Boatwright (2002), 2: Seismic sources and source parameters, in *IASPEI New Manual of Seismological Observatory Practice*, vol. 1, edited by P. Bormann, chap. 3, p. 36, GeoForschungsZentrum Potsdam, Potsdam, Germany.

Bratt, S. R., E. A. Bergman, and S. C. Solomon (1985), Thermoelastic stress: How important as a cause of earthquakes in young oceanic lithosphere?, *J. Geophys. Res.*, *90*, 10,249–10,260.

Bryan, W. B. (1973), Wrinkle ridges as deformed surface crust on ponded mare lava, *Proc. Lunar Planet. Sci. Conf.*, *4th*, 93–106.

Cailleau, B., T. R. Walter, P. Janle, and E. Hauber (2003), Modeling volcanic deformation in a regional stress field: Implications for the formation of graben structures on Alba Patera, Mars, *J. Geophys. Res.*, *108*(E12), 5141, doi:10.1029/2003JE002135.

Carr, M. H. (1974), Tectonism and volcanism of the Tharsis region of Mars, *J. Geophys. Res.*, *79*, 3943–3949.

Carr, M. H. (1981), *The Surface of Mars*, 232 pp., Yale Univ. Press, New Haven.

Chicarro, A. F., P. H. Schultz, and P. Masson (1985), Global and regional ridge patterns on Mars, *Icarus*, *63*, 153–174.

Davis, P. M. (1993), Meteoroid impacts as seismic sources on Mars, *Icarus*, *105*, 469–478.

Davis, P. A., and M. P. Golombek (1989), Dioscontinuities in the Shallow Martian Crust, *Lunar Planet. Sci. Conf.*, *XX*, 224.

Deuchler, C., M. Wählisch, S. Gehrke, E. Hauber, J. Oberst, and R. Jaumann (2004), Combining Mars data in GRASS for geological mapping paper presented at XXth Congress ISPRS, Int. Soc. for Photogramm. and Remote Sens., Istanbul, Turkey, 12–23 July.

Dohm, J. M., and K. L. Tanaka (1999), Geology of the Thaumasia region, Mars: Plateau development, valley origins, and magmatic evolution, *Planet. Space Sci.*, *47*, 411–431.

Dziewonski, A. M., and D. L. Anderson (1981), Preliminary Reference Earth Model, *Phys. Earth Planet. Inter.*, *25*, 297–356.

Dziewonski, A. M., and J. H. Woodhouse (1983), An experiment in the systematic study of global seismicity: Centroid-moment tensor solutions for 201 moderate and large earthquakes of 1981, *J. Geophys. Res.*, *88*, 3247–3271.

Dziewonski, A. M., A. Friedman, D. Giardini, and J. H. Woodhouse (1983), Global seismicity of 1982: Centroid-moment tensor solutions for 308 earthquakes, *Phys. Earth Planet. Inter.*, *33*, 76–90.

Frey, H. V., B. G. Bills, R. S. Nerem, and J. H. Roark (1996), The isostatic state of Martian topography revisited, *Geophys. Res. Lett.*, *23*, 721–724.

Frigeri, A., C. Federico, G. Minelli, C. Pauselli, and C. Caldarella (2002), Identifying wrinkle ridges structures from Mars MGS and Viking Mission Data: Using GRASS in planetary geology paper presented at Open Source GIS–GRASS Users Conference 2002, Univ. of Trento, Trento, Italy.

Fujii, Y., and M. Matsu'ura (2000), Regional difference in scaling laws for large earthquakes and its tectonic implication, *Pure Appl. Geophys.*, *157*, 2283–2302.

Godano, C., and F. Pingue (2000), Is the Seismic moment-frequency relation universal?, *Geophys. J. Int.*, *142*, 193–198.

Goins, N. R., and A. R. Lazarewicz (1979), Martian seismicity, *Geophys. Res. Lett.*, *6*, 368–370.

Goins, N. R., A. M. Dainty, and M. Nafi Toksöz (1981), Seismic energy release of the Moon, *J. Geophys. Res.*, *86*, 378–388.

Golombek, M. P. (1994), Constraints on the Largest Marsquake, *Lunar Planet. Sci. Conf.*, *XXV*, 441.

Golombek, M. P. (2002), A revision of Mars seismicity from surface faulting, *Lunar Planet. Sci. Conf.*, *XXXIII*, Abstract 1244.

Golombek, M. P., W. B. Banerdt, K. L. Tanaka, and D. M. Tralli (1992), A prediction of Mars seismicity from surface faulting, *Science*, *258*, 979–981.

Golombek, M. P., F. S. Anderson, and M. T. Zuber (2001), Martian wrinkle ridge topography: Evidence for subsurface faults from MOLA, *J. Geophys. Res.*, *106*, 23,811–23,821.

Grott, M., E. Hauber, S. C. Werner, P. Kronberg, and G. Neukum (2005), High heat flux on ancient Mars: Evidence from rift flank uplift at Coracis Fossae, *Geophys. Res. Lett.*, *32*, L21201, doi:10.1029/2005GL023894.

Gupta, A., and C. H. Scholz (2000), Brittle strain regime transition in the Afar depression: Implications for fault growth and seafloor spreading, *Geology*, *28*, 1087–1090.

Hartmann, W. K., and G. Neukum (2001), Cratering chronology and the evolution of Mars, *Space Sci. Rev.*, *96*, 165–194.

Hartmann, W. K., et al. (1981), Chronology of planetary volcanism by comparative studies of planetary cratering, in *Basaltic Volcanism on the Terrestrial Planets*, edited by W. M. Kaula, R. B. Merrill and R. Ridings, pp. 1049–1127, Elsevier, New York.

Hauber, E., and P. Kronberg (2001), Tempe Fossae, Mars: A planetary analogon to a terrestrial continental rift?, *J. Geophys. Res.*, *106*, 20,587–20,602.

Hauber, E., and P. Kronberg (2005), The large Thaumasia graben on Mars: Is it a rift?, *J. Geophys. Res.*, *110*, E07003, doi:10.1029/2005JE002407.

Hauck, S. A., S. C. Solomon, and R. J. Phillips (2003), Potential sources of Hesperian contractional tectonics on Mars, *Lunar Planet. Sci. Conf.*, *XXXIV*, Abstract 1667.

Ivanov, B. A. (2001), Mars/Moon cratering rate ratio estimates, *Space Sci. Rev.*, *96*, 87–104.

Kagan, Y. Y. (1997), Seismic moment-frequency relation for shallow earthquakes: Regional comparison, *J. Geophys. Res.*, *102*, 2835–2852.

Kagan, Y. Y. (1999), Universality of the seismic moment-frequency relation, *Pure Appl. Geophys.*, *155*, 537–573.

Kagan, Y. Y. (2002a), Seismic moment distribution revisited: I. Statistical results, *Geophys. J. Int.*, *148*, 520–541.

Kagan, Y. Y. (2002b), Seismic moment distribution revisited: II. Moment conservation principle, *Geophys. J. Int.*, *149*, 731–754.

Kanamori, H. (1994), Mechanics of earthquakes, *Annu. Rev. Earth Planet. Sci.*, *22*, 207–237.

Kanamori, H., and D. L. Anderson (1975), Theoretical basis of some empirical relations in seismology, *Bull. Seismol. Soc. Am.*, *65*, 1073–1095.

Kim, Y.-S., and D. J. Sanderson (2005), The relationship between displacement and length of faults: A review, *Earth Sci. Rev.*, *68*, 317–334.

Kirk, R. L., E. M. Lee, R. M. Sucharski, J. Richie, A. Grecu, and S. K. Castro (2000), MDIM 2.0: A revised global digital image mosaic of Mars, *Lunar Planet. Sci. Conf.*, *XXXI*, Abstract 2011.

Lognonné, P. (2005), Planetary seismology, *Annu. Rev. Earth Planet. Sci.*, *33*, 571–604.

Lognonné, P., et al. (2000), The NetLander very broad band seismometer, *Planet. Space Sci.*, *48*, 1289–1302.

Liu-Zeng, J., T. Heaton, and C. DiCaprio (2005), The effect of slip variability on earthquake slip-length scaling, *Geophys. J. Int.*, *162*, 841–849.

Mansfield, C., and J. Cartwright (2001), Fault growth by linkage: Observations and implications from analogue models, *J. Struct. Geol.*, *23*, 745–763.

Marrett, R. (1996), Aggregate properties of fracture populations, *J. Struct. Geol.*, *18*, 169–178.

Marrett, R., and R. W. Allmendinger (1992), Amount of extension on "small" faults: An example from the Viking graben, *Geology*, *20*, 47–50.

Maxwell, T. A., F. El-Baz, and S. W. Ward (1975), Distribution, morphology, and origin of ridges and arches in Mare Serenitatis, *Geol. Soc. Am. Bull.*, *86*, 1273–1278.

McGarr, A. (1976), Upper limit to earthquake size, *Nature*, *262*, 378–379.

McGovern, P. J., S. C. Solomon, D. E. Smith, M. T. Zuber, M. Simons, M. A. Wieczorek, R. J. Phillips, G. A. Neumann, O. Aharonson, and J. W. Head (2002), Localized gravity/topography admittance and correlation spectra on Mars: Implications for regional and global evolution, *J. Geophys. Res.*, *107*(E12), 5136, doi:10.1029/2002JE001854.

McGovern, P. J., S. C. Solomon, D. E. Smith, M. T. Zuber, M. Simons, M. A. Wieczorek, R. J. Phillips, G. A. Neumann, O. Aharonson, and J. W. Head (2004), Correction to "Localized gravity/topography admittance and correlation spectra on Mars: Implications for regional and global evolution," *J. Geophys. Res.*, *109*, E07007, doi:10.1029/2004JE002286.

Mocquet, A. (1999), A search for the minimum number of stations needed for seismic networking on Mars, *Planet. Space Sci.*, *47*, 397–409.

Mocquet, A., P. Vacher, O. Grasset, and C. Sotin (1996), Theoretical seismic models of Mars: The importance of the iron content of the mantle, *Planet. Space Sci.*, *44*, 1251–1268.

Mueller, K., and M. P. Golombek (2004), Compressional structures on Mars, *Annu. Rev. Earth Planet. Sci.*, *32*, 435–464.

Neukum, G., and K. Hiller (1981), Martian ages, *J. Geophys. Res.*, *86*, 3097–3121.

Neukum, G., and D. U. Wise (1976), Mars: A standard crater curve and possible new time scale, *Science*, *194*, 1381–1387.

Neukum, G., B. A. Ivanov, and W. K. Hartmann (2001), Cratering records in the inner solar system in relation to the lunar reference system, in *Chronology and Evolution of Mars*, edited by W. K. Hartmann, J. Geiss, and R. Kallenbach, pp. 53–86, Springer, New York.

Neukum, G., et al. (2004), Recent and episodic volcanic and glacial activity on Mars revealed by the high resolution stereo camera, *Nature*, *432*, 971–979.

Nicol, A., J. Watterson, J. J. Walsh, and C. Childs (1996), The shapes, major axis orientations and displacement patterns of fault surfaces, *J. Struct. Geol.*, *18*, 235–248.

Nimmo, F., and K. Tanaka (2005), Early crustal evolution of Mars, *Annu. Rev. Earth Planet. Sci.*, *33*, 133–161.
Oberst, J. (1987), Unusually high stress drops associated with shallow moonquakes, *J. Geophys. Res.*, *92*, 1397–1405.
Okubo, C. H., and R. A. Schultz (2004), Temporal variability in Tharsis stress state based on wrinkle ridges and strike-slip faulting [CD-ROM], *Lunar Planet. Sci.*, *XXXV*, Abstract 1101.
Peacock, D. C. P. (2002), Propagation, interaction and linkage in normal fault systems, *Earth Sci. Rev.*, *58*, 121–142.
Phillips, R. J. (1991), Expected rates of Marsquakes, in *Scientific Rationale and Requirements for a Global Seismic Network on Mars*, *LPI Tech. Rep. 91–02 LPI/TR-91–02*, pp. 35–38, Lunar and Planet. Inst., Houston, Tex.
Phillips, R. J., and R. E. Grimm, (1991), Martian seismicity, *Lunar Planet. Sci. Conf.*, *XXII*, Abstract 1061.
Plescia, J. B., and R. S. Saunders (1982), Tectonic history of the Tharsis region, Mars, *J. Geophys. Res.*, *87*, 9775–9791.
Pounders, E., R. C. Anderson, J. M. Dohm, A. F. C. Haldemann, and M. P. Golombek (2002), Tectonic evolution of the eastern hemisphere of Mars, *Lunar Planet. Sci. Conf.*, *XXXIII*, Abstract 1906.
Schlische, R. W., S. S. Young, R. V. Ackermann, and A. Gupta (1996), Geometry and scaling relations of a population of very small rift-related faults, *Geology*, *24*(8), 683–686.
Scholz, C. H. (1998), Earthquakes and friction laws, *Nature*, *391*, 37–42.
Scholz, C. H. (2003), *The Mechanics of Earthquakes and Faulting*, 2nd ed., 471 pp., Cambridge Univ. Press, New York.
Schultz, R. A. (1989), Strike-slip faulting of ridged plains near Valles Marineris, Mars, *Nature*, *341*, 424–426.
Schultz, R. A. (2000a), Localization of bedding plane slip and backthrust faults above blind thrust faults: Keys to wrinkle ridge structure, *J. Geophys. Res.*, *105*, 12,035–12,052.
Schultz, R. A. (2000b), Fault-population statistics at the Valles Marineris Extensional Province, Mars: Implications for segment linkage, crustal strains, and its geodynamical development, *Tectonophysics*, *316*, 169–193.
Schultz, R. A. (2003), Seismotectonics of the Amenthes Rupes thrust fault population, Mars, *Geophys. Res. Lett.*, *30*(6), 1303, doi:10.1029/2002GL016475.
Schultz, R. A., and A. N. Fori (1996), Fault-length statistics and implications of graben sets at Candor Mensa, Mars, *J. Struct. Geol.*, *18*, 373–383.
Schultz, R. A., and J. Lin (2001), Three-dimensional normal faulting of the Valles Marineris, Mars, and geodynamic implications, *J. Geophys. Res.*, *106*, 16,549–16,566.
Schultz, R. A., and T. R. Watters (2001), Forward mechanical modeling of the Amenthes Rupes thrust fault on Mars, *Geophys. Res. Lett.*, *28*, 4659–4662.
Schumacher, S., and D. Breuer (2006), Influence of a variable thermal conductivity on the thermochemical evolution of Mars, *J. Geophys. Res.*, *111*, E02006, doi:10.1029/2005JE002429.
Scott, D. H., K. L. Tanaka, R. Greeley, and J. E. Guest (1986), Geologic map of the western equatorial region of Mars, *U.S. Geol. Surv. Misc. Invest. Ser. Map, I-1802-A*.
Scott, D. H., K. L. Tanaka, R. Greeley, and J. E. Guest (1987a), Geologic map of the eastern equatorial region of Mars, *U.S. Geol. Surv. Misc. Invest. Ser. Map, I-1802-B*.
Scott, D. H., K. L. Tanaka, R. Greeley, and J. E. Guest (1987b), Geologic map of the polar regions of Mars, *U. S. Geol. Surv. Misc. Invest. Ser. Map, I-1802-C*.
Shaw, B. E., and C. H. Scholz (2001), Slip-length scaling in large earthquakes: Observations and theory and implications for earthquake physics, *Geophys. Res. Lett.*, *28*, 2991–2994.
Smith, D. E., et al. (1999), The global topography of Mars and implications for surface evolution, *Science*, *284*, 1495–1503.
Smith, D. E., et al. (2001), Mars Orbiter laser altimeter: Experiment summary after the first year of global mapping of Mars, *J. Geophys. Res.*, *106*, 23,689–23,722.
Smith, D. E., G. Neumann, R. E. Arvidson, E. A. Guiness, and S. Slavney (2003), Mars Global Surveryor Laser Altimeter Mission Experiment Gridded Data Record, MGS-M-MOLA-5-MEGDR-L3-V1.0, http://starbrite.jpl.nasa.gov/pds-explorer/dsidnode.jsp?nodename=GEOSCIENCE&datasetid=MGS-M-MOLA-5-MEGDR-L3-V1.0, NASA Planet. Data Syst., Greenbelt, Md.
Sohl, F., and T. Spohn (1997), The interior structure of Mars: Implications from SNC meteorites, *J. Geophys. Res.*, *102*, 1613–1635.
Stacey, F. D. (1992), *Physics of the Earth*, 3rd ed., Brookfield, Kenmore, Queensl., Australia.
Starr, A. T. (1928), Slip in a *Crystal and Rupture in a Solid due to Shear*, *Proc. Cambridge Philos. Soc.*, *24*, 489–500.
Stein, S., and C. A. Stein (1996), Thermo-mechanical evolution of oceanic lithosphere: Implications for the subduction process and deep earthquakes, in *Subduction Top to Bottom*, *Geophys. Monogr. Ser.*, vol. 96, edited by G. E. Bebout et al., pp. 1–17, AGU, Washington, D. C.
Stevenson, D. J. (2001), Mars' core and magnetism, *Nature*, *412*, 214–219.
Strom, R. G. (1972a), Lunar mare ridges, rings, and volcanic ring complexes, *Mod. Geol.*, *2*, 133–157.
Strom, R. G. (1972b), Lunar mare ridges, rings, and volcanic ring complexes, in *The Moon*, edited by S. K. Runcorn and H. C. Urey, pp. 187–215, Springer, New York.
Tanaka, K. L. (1986), The stratigraphy of Mars, *Proc. Lunar Planet Sci. Conf. 17th*, Part 1, *J. Geophys. Res.*, *91*, suppl., E139–E158.
Tanaka, K. L. (1990), Tectonic history of the Alba Patera-Ceraunius Fossae region of Mars, *Proc. Lunar Planet. Sci. Conf.*, *20th*, 515–523.
Tanaka, K. L., and P. A. Davis (1988), Tectonic history of the Syria Planum province of Mars, *J. Geophys. Res.*, *93*, 14,893–14,917.
Tanaka, K. L., M. P. Golombek, and W. B. Banerdt (1991), Reconciliation of stress and structural histories of the Tharsis region of Mars, *J. Geophys. Res.*, *96*, 15,617–15,633.
Tanaka, K. L., D. H. Scott and R. Greeley (1992), Global stratigraphy, in *Mars*, edited by H. H. Kieffer et al., pp. 345–382, Univ. of Ariz. Press.
Tanaka, K. L., J. A. Skinner, T. M. Hare, T. Joyal, and A. Wenker (2003), Resurfacing history of the northern plains of Mars based on geologic mapping of Mars Global Surveyor data, *J. Geophys. Res.*, *108*(E4), 8043, doi:10.1029/2002JE001908.
Turcotte, D. L., R. Shcherbakov, B. D. Malamud, and A. B. Kucinskas (2002), Is the Martian crust also the Martian elastic lithosphere?, *J. Geophys. Res.*, *107*(E11), 5091, doi:10.1029/2001JE001594.
Walsh, J. J., and J. Watterson (1992), Populations of faults and fault displacements and their effects on estimates of fault-related regional extension, *J. Struct. Geol.*, *14*, 701–721.
Ward, S. N. (1998a), On the consistency of earthquake moment rates, geological fault data, and space geodetic strain: The United States, *Geophys. J. Int.*, *134*, 172–186.
Ward, S. N. (1998b), On the consistency of earthquake moment rates, geological fault data, and space geodetic strain: Europe, *Geophys. J. Int.*, *135*, 1011–1018.
Watters, T. R. (1993), Compressional tectonism on Mars, *J. Geophys. Res.*, *98*, 17,049–17,060.
Watters, T. R. (2003), Thrust faults along the dichotomy boundary in the eastern hemisphere of Mars, *J. Geophys. Res.*, *108*(E6), 5054, doi:10.1029/2002JE001934.
Watters, T. R., and M. S. Robinson (1999), Lobate scarps and the Martian crustal dichotomy, *J. Geophys. Res.*, *104*, 18,981–18,990.
Watters, T. R., R. A. Schultz, and M. S. Robinson (2000), Displacement-length relations of thrust faults associated with lobate scarps on Mercury and Mars: Comparison with terrestrial faults, *Geophys. Res. Lett.*, *27*, 3659–3662.
Wells, D. L., and K. J. Coppersmith (1994), New empirical relationships among magnitude, rupture length, rupture width, rupture area, and surface displacement, *Bull. Seismol. Soc. Am.*, *84*, 974–1002.
Westerhaus, M., M. Wyss, R. Yilmaz, and J. Zschau (2002), Correlating variations of *b* values and crustal deformations during the 1990s may have pinpointed the rupture initiation of the *Mw* = 7. 4 Izmit earthquake of 1999 August 17, *Geophys. J. Int.*, *148*, 139–152.
Wilkins, S. J., and R. A. Schultz (2003), Cross faults in extensional settings: Stress triggering, displacement localization, and implications for the origin of blunt troughs at Valles Marineris, Mars, *J. Geophys. Res.*, *108*(E6), 5056, doi:10.1029/2002JE001968.
Wilkins, S. J., R. A. Schultz, R. C. Anderson, J. M. Dohm, and N. H. Dawers (2002), Deformation rates from faulting at the Tempe Terra extensional province, Mars, *Geophys. Res. Lett.*, *29*(18), 1884, doi:10.1029/2002GL015391.
Wise, D. U., M. P. Golombek, and G. E. McGill (1979), Tectonic evolution of Mars, *J. Geophys. Res.*, *84*, 7934–7939.
Yielding, G., J. J. Walsh, and J. Watterson (1992), The prediction of small-scale faulting in reservoirs, *First Break*, *10*, 449–460.
Yielding, G., T. Needham, and H. Jones (1996), Sampling of fault populations using sub-surface data: A review, *J. Struct. Geol.*, *18*, 135–146.
Zhong, S. (2002), Effects of lithosphere on the long-wavelength gravity anomalies and their implications for the formation of the Tharsis rise on Mars, *J. Geophys. Res.*, *107*(E7), 5054, doi:10.1029/2001JE001589.
Zuber, M. T. (2001), The crust and mantle of Mars, *Nature*, *412*, 220–227.
Zuber, M. T., et al. (2000), Internal structure and early thermal evolution of Mars from Global Surveyor topography and gravity, *Science*, *287*, 1788–1893.

C. Deuchler, E. Hauber, M. Knapmeyer, J. Oberst, M. Wählisch, and R. Wagner, German Aerospace Center, Institute of Planetary Research, Rutherfordstrasse 2, D-12489 Berlin, Germany. (martin.knapmeyer@dlr.de)